The Journal of Acoustical Society of India

Volume 52 Number 1 January 2025 pp 1-41

ISSN 0973-3302

THE JOURNAL OF ACOUSTICAL SOCIETY OF INDIA

Volume 52 Number 1 January 2025

A Quarterly Publication of the ASI
https://acoustics.org.in

ASI

The Journal of Acoustical Society of India

The Refereed Journal of the Acoustical Society of India (JASI)

The Journal of Acoustical Society of India is a refereed journal of the Acoustical Society of India **(ASI)**. The **ASI** is a non-profit national society founded in 31st July, 1971. The primary objective of the society is to advance the science of acoustics by creating an organization that is responsive to the needs of scientists and engineers concerned with acoustics problems all around the world.

Manuscripts of articles, technical notes and letter to the editor should be submitted to the Chief Editor. Copies of articles on specific topics listed above should also be submitted to the respective Associate Scientific Editor. Manuscripts are refereed by at least two referees and are reviewed by Publication Committee (all editors) before acceptance. On acceptance, revised articles with the text and figures scanned as separate files on a diskette should be submitted to the Editor by express mail. Manuscripts of articles must be prepared in strict accordance with the author instructions.

All information concerning subscription, new books, journals, conferences, etc. should be submitted to Chief Editor:

B. Chakraborty, CSIR - National Institute of Oceanography, Dona Paula, Goa-403 004,
Tel: +91.832.2450.318, Fax: +91.832.2450.602, e-mail: bishwajit@nio.org

Annual subscription price including mail postage is Rs. 2500/= for institutions, companies and libraries and Rs. 2500/= for individuals who are not **ASI** members. The Journal of Acoustical Society of India will be sent to **ASI** members free of any extra charge. Requests for specimen copies and claims for missing issues as well as address changes should be sent to the Editorial Office:

ASI Secretariat, C/o Acoustics and Vibration Metrology, CSIR-National Physical Laboratory, Dr. KS Krishnan Road, New Delhi 110 012, Tel: +91.11.4560.8317, Fax: +91.11.4560.9310, e-mail: asisecretariat.india@gmail.com

ISSN 0973-3302

Printed at Alpha Printers, WZ-35/C, Naraina, Near Ring Road, New Delhi-110028 Tel.: 9810804196. JASI is sent to ASI members free of charge.

The Journal of Acoustical Society of India

A quarterly publication of the Acoustical Society of India

Volume 52, Number 1, January 2025

ARTICLES

INFORMATION

FOREWORD

We are elated to bring out this special issue of Journal of Acoustical Society of India devoted to the theme 'Vibroacoustics' with emphasis on Vibration & Noise Prediction and Analysis. The subject of Vibroacoustics is a study of interplay between vibration and sound. It can be seen as a study that integrates analysis of mechanical vibrations and sound to understand their interaction. Research on Vibration and noise simulation spans from analytical treatments, empirical models to advanced numerical methods. Analytical approach with closed form solution is always academician's delight and hence, where possible, this approach is adopted by researchers. Advent of advanced computational methods particularly Finite Element Method and Computational Fluid Mechanics made it possible to predict Vibration and Noise very accurately. On the other hand, experimental studies also can provide estimation of vibration behaviour of structures including those bonded with smart materials. Empirical approach provides another alternative of estimation of noise by dovetailing certain experimental information in mathematical models. It is also pertinent to note that Sound, structure and their interaction has been a topic of great interest for many years.

This special issue has contributed papers on Propeller non cavitating noise prediction, Coupled analysis of water loaded unbaffled plate, Vibration analysis of beams bonded with smart sensors, Empirical model to predict ball bearing noise and sound structure interaction in a 2D flexible wave guide. We wish to thank all the authors for their contribution to this special issue.

PVS Ganesh Kumar
Outstanding Scientist/Scientist H (Retd)

Dr.V Rama Krishna
Scientist 'F'
Naval Science & Technological Laboratory (NSTL)
Defense R&D Organisation (DRDO)
Ministry of Defence, Visakhapatnam - 530 027

The Journal of Acoustical Society of India : Vol. 52, No. 1, 2025 (pp. 1-10)

Noise prediction of DTMB-4119 propeller in non-cavitating condition

V. Ramakrishna[1*] and Rejith Nair Rajeev[2]
[1]*Naval Science and Technological Laboratory (NSTL), DRDO,*
Vigyan Nagar, Visakhapatnam-530 027, India
[2]*Department of Electronics,*
Cochin University of Science and Technology (CUSAT), Kochi-682 022, India
e-mail: ramki40@gmail.com

[Received: 05-05-2025; Accepted: 22-08-2025]

ABSTRACT

The objective of this study is to utilize computational fluid dynamic (CFD) to predict the underwater noise characteristics of DTMB 4119 propeller. Due to the propeller's major influence on the noise produced by marine vessels, a hydro-acoustic study utilizing unsteady RANS with the F fowcs-Williams and Hawkings (FW-H) equation is carried out. Underwater acoustic level of the propeller is determined through CFD using FW-H; and the Overall Sound Pressure Level (OASPL) values are computed using a semi-empirical formula. The OASPL values obtained from both these methods are compared to understand the underwater acoustics of the propeller. For this analysis, the flow is treated as an unsteady, incompressible flow, and the Reynolds Averaged Navier-Stokes (RANS) equations are used to solve the problem.

1. INTRODUCTION

A vessel with the ability to operate independently underwater is known as a submarine (or sub). The term is also sometimes used colloquially to refer to remotely operated vehicles and robots, as well as medium-sized or smaller vessels. Submarines are referred to as boats rather than ships irrespective of their size. For designers of contemporary naval warfare, submarines are an essential component of maritime strategy. Their contributions to sea control, sea denial, and maritime force projection-the three pillars of maritime operational warfare-are very important. Because they are an essential part of any significant naval power's order of battle and because surface forces facing a submarine threat must assemble a complex, costly, and fragile defence system, medium and small fleets are rapidly acquiring them. Submarines are not only used for anti-submarine warfare, but they also are used for reconnaissance and rescue operations, as well as for laying mines.

There are several differences between submarines, including size, propulsion, and armament. Creating a submarine is regarded as one of the trickiest military projects. This is so because a submarine is a metal container that is sealed and holds humans along with a finite amount of air. Because they can only be built to a certain size, they are packed with of supplies, weaponry, and equipment. When it comes to submarine design, the challenge for a naval architect is increasing the hydrodynamic performance of these underwater vessels in terms of resistance, propulsion, maneuverability, stability, and stealth. Designing them for stealth is particularly difficult because of the diverse operating conditions and mission requirements. Therefore, it is essential to accurately predict and reduce the overall noise levels. This study's goal is to do a computational fluid dynamic analysis of the DTMB 4119 propeller to predict the noise levels at different RPMs.

The impact of the number of blades, diameter, and rotation speed on the sound pressure level is examined by Soydan *et al.*[1]. A highly useful and straightforward approach, based on the semi-empirical Brown formula, is also provided for non-cavitating maritime propellers. In this study, the noise from the DTMB-4119 propeller is predicted using RANS and OASPL equation and the sound pressure values are compared. Esteves *et al.*[2] obtained propulsive coefficients of submarines from three sets of simulations: traditional method, virtual disk model coupled to the bare hull and the propeller hull interaction in a single fluid domain. The bare hull and virtual disk model simulations have low computational cost but require the open water propeller simulations. The authors concluded that the complete simulation guarantees a better definition of the propeller-hull coupling and interference, but with higher computational cost. The INSEAN E1619 submarine propeller is investigated numerically by Ozden *et al.*[3] in open water, behind a typical DARPA suboff submarine, and in induced wake situations under non-cavitating circumstances. The hydrodynamic noise produced by the flow surrounding a non-cavitating underwater propeller was numerically simulated by Mousavi *et al.*[4]. The LES turbulence model and unsteady 3-D flow were both numerically modelled, and the results were compared with earlier experimental studies. Through a comparison with experimental measures, Gaggero *et al.*[5] demonstrated the strengths and weaknesses of two distinct numerical approaches-a commercial RANS solver and an in-house developed Panel Method-applied to the analysis of marine propellers subjected to an oblique inflow.

2. PROPELLER NOISE PREDICTION

The objective is to assess the noise generated by the DTMB 4119 propeller in different operating conditions, with a focus on determining the Propeller Overall Sound Pressure Level (OASPL). URANS is used to model the flow around the propeller and to obtain information about the unsteady pressure fluctuations generated by the rotating blades. FW-H equation is employed to convert these pressure fluctuations into acoustic signals. This equation, a fundamental tool in computational acoustics, allows to estimate the radiated acoustic field from the computed flow data. It takes into account the unsteady flow properties, such as velocity and pressure, and calculates the acoustic pressure at a specified distance from the source.

3. GEOMETRY MODELING AND MESHING

DTMB 4119 propeller was modeled using CAESES software. The standard design table for the propeller, which has camber line, a=0.8 is shown in Table 1 and a NACA 66 modified profile is shown in Fig.1.

A cylindrical fluid domain model of length and diameter 2100 mm and 900 mm was created. Since the underwater noise signals have to be captured; receivers are positioned at 1m distance around the propeller as shown in Fig. 2.

Table 1. Design parameters of the NACA 66 blade.

r/R	c/D	rk/D	sk(°)	P/D	t_{max}/c	f_{max}/c
0.20	0.3200	0.00	0.00	1.1050	0.2055	0.0143
0.30	0.3635	0.00	0.00	1.1022	0.1553	0.0232
0.40	0.4048	0.00	0.00	1.0983	0.1180	0.0230
0.50	0.4392	0.00	0.00	1.0932	0.0902	0.0218
0.60	0.4610	0.00	0.00	1.0879	0.0696	0.0207
0.70	0.4622	0.00	0.00	1.0839	0.0542	0.0200
0.80	0.4347	0.00	0.00	1.0811	0.0421	0.0197
0.90	0.3613	0.00	0.00	1.0785	0.0332	0.0182
0.95	0.2775	0.00	0.00	1.0770	0.0323	0.0163
0.98	0.2045	0.00	0.00	1.0761	0.0321	0.0145
1.00	0.0800	0.00	0.00	1.0750	0.0316	0.0118

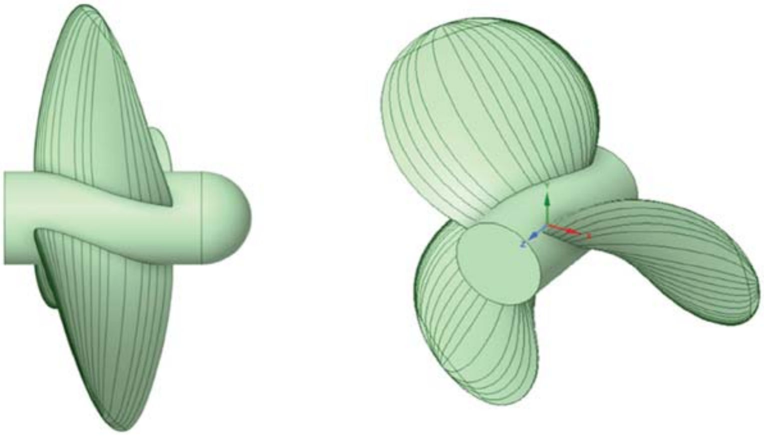

Fig. 1. DTMB 4119 propeller model.

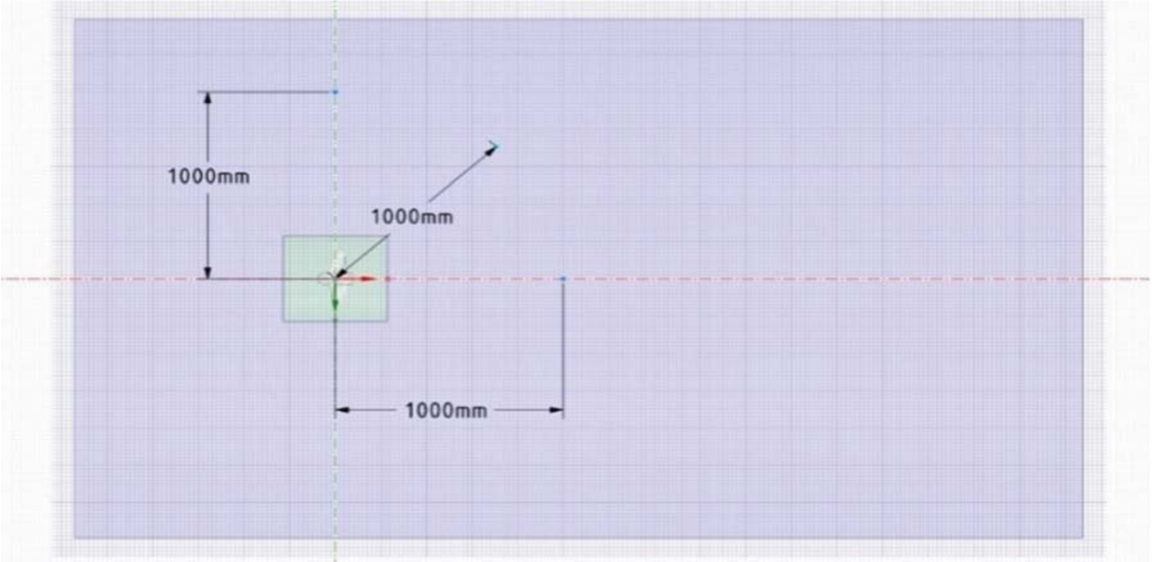

Fig. 2. Receiver locations in the propeller domain.

In the FLUENT meshing program, polyhedral meshing was carried out for the propeller domain. Based on the change in Reynolds number, four alternative meshes were chosen. Therefore, there were between 5 and 10 million elements. It was decided to keep the first layer's thickness between 9.95 to 2.27 microns so that the Y+ could always be kept below 10. Fig 3 and 4 show the polyhedral element-based mesh.

4. PRESSURE CONTOURS AND FIRST LAYER THICKNESS

Simulation results obtained from the CFD analysis are presented as pressure contours and Y+ values at different velocities as shown in Fig. 5 and 6 respectively.

For the K-omega model, the Y^+ has to be always maintained below 10, and this is possible only if the first layer thickness is calculated based on the viscous model requirement. Equation (1) to (5) are used for this purpose.

$$\text{First layer thinkness y isdefined as :} \frac{y^{+*\mu}}{\mu_{fr*\rho}} \tag{1}$$

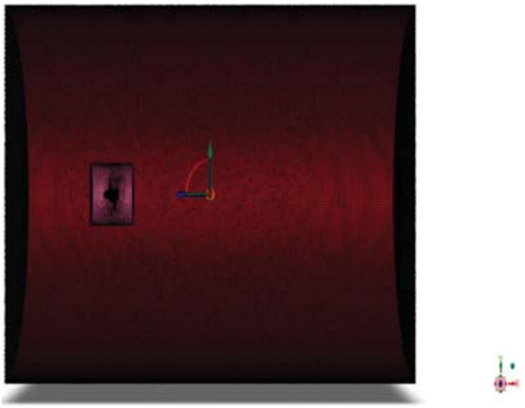

Fig. 3. Mesh structure of the propeller domain.

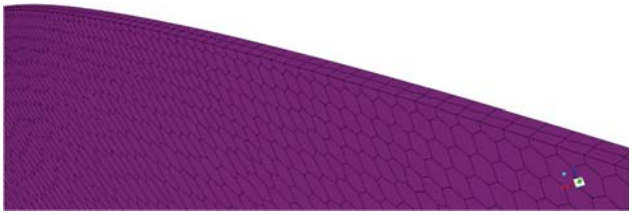

Fig. 4. Mesh structure at the tip of the propeller blade.

Table 2. Pre-processing conditions.

Flow Parameters	
Axial velocity (V_A)	2.539 m/s, 3.808 m/s, 5.078 m/s, 10.156 m/s
Advance coefficient	J=0.833
RPMs	600, 900, 1200, 2400
Seawater density	1025 kg/m^3
Modeling	
Viscous Model	K-Ω SST
Acoustic Model	F fowcs Williams and Hawkings (FW-H) formulation
Reference Acoustic Pressure	1μPa
Far-field sound speed	1500 m/s
Sound sources	Rotor domain walls
Boundary Conditions	
Inlet (upstream domain face)	Velocity inlet
Far-field (walls)	Velocity inlet
Outlet (downstream face)	Pressure outlet
Stators-rotor-Inlet (downstream face)	Pressure inlet
Stators-rotor- Far-field (Stator domain walls)	Interface
Stators-rotor Outlet (upstream face)	Pressure outlet
Rotor Inlet (upstream face)	Pressure inlet
Rotor Far-field (domain walls)	Interface
Rotor Outlet (downstream face)	Pressure outlet
Numerical scheme	
Solver	Momentum-based
Pressure velocity coupling:	SIMPLEC
Spatial discretization:	Gradient least square cell based
Pressure discretization:	Second Order
Momentum discretization:	Second Order Upwind
Turbulent Kinetic and specific dissipation energy rate discretization:	Second Order Upwind

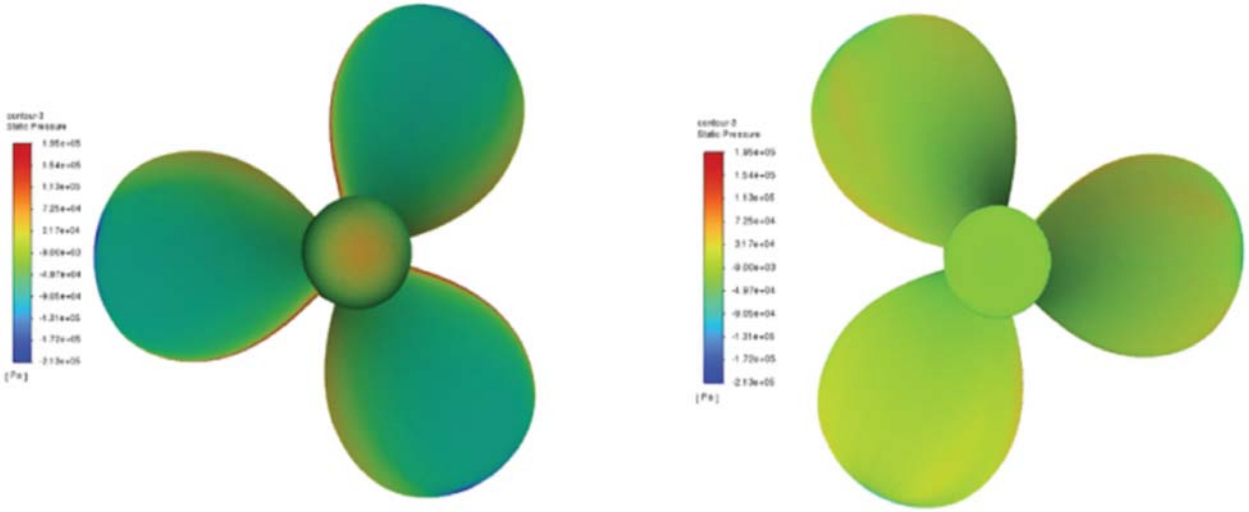

Fig. 5. Pressure contours of the propeller at inlet (left) and outlet (right).

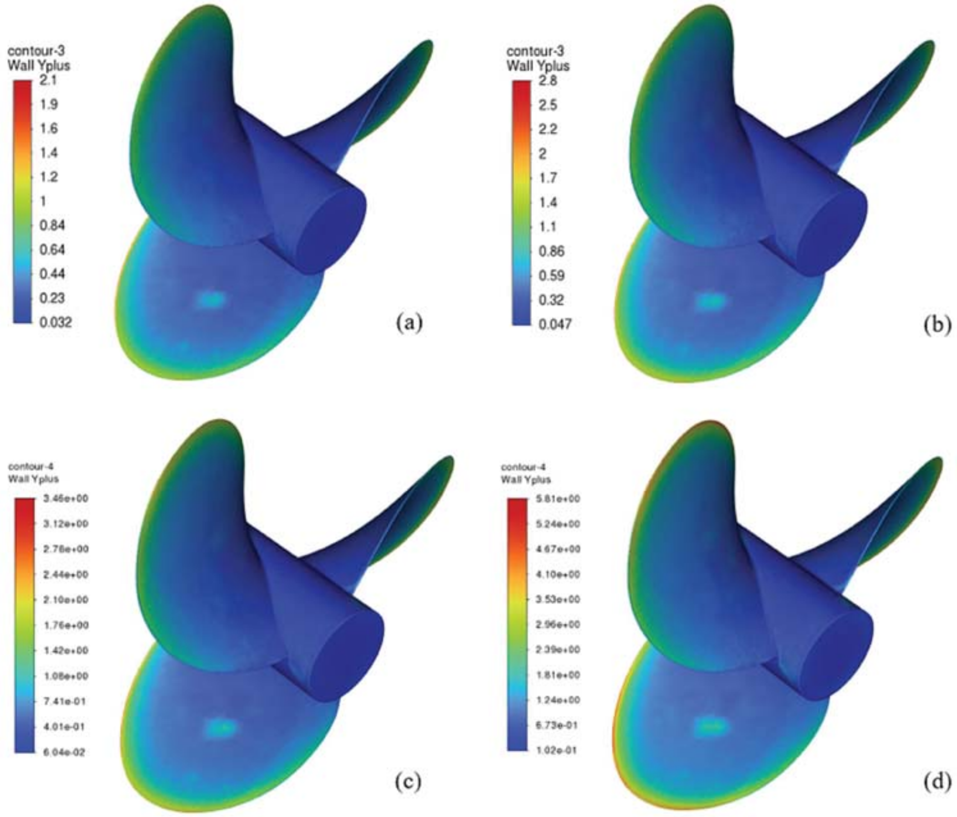

Fig. 6. Y+ values at different velocities (a) 2.539 m / s; max Y+2.1 (b) 3.808 m / s; max Y+ 2.8 (c) 5.078 m / s; max Y+ 3.46 (d) 10.156 m / s; max Y+ 5.81

Where, $y^+ = 1$, $\mu = 1.20e\text{-}3$, $\rho = 1026$ kg / m^3

$$\mu_{fr} = \sqrt{\frac{\tau_{wall}}{\rho}} \tag{2}$$

$$\tau_{wall} = \frac{C_f * \rho * \upsilon^2}{2} \tag{3}$$

$$C_f = \frac{0.026}{2} \tag{4}$$

$$\Re_{\text{propeller}} = \frac{\rho C_{0.7R}\sqrt{\upsilon^2 + (n\pi * 0.7D)^2}}{\mu} \tag{5}$$

Where,

$C_{0.7R}$ = 0.14 m for the DTMB 4119 propeller & D = 0.3 m

Table 3 shows the calculated first layer thickness for K-Ω model at different velocities.

Table 3. Calculation of first layer thickness for K-Ω model.

V (m/s)	Re	Cf	τ_{wall}	${}_{\mu}fr$	y(m)
2.539	3.04E+05	4.28E-03	14.162	0.117	0.000009955
3.808	4.56E+05	4.04E-03	30.065	0.171	0.000006832
5.078	6.08E+05	3.88E-03	51.310	0.223	0.000005230
10.156	1.22E+06	3.51E-03	185.891	0.425	0.000002748

5. ACOUSTIC NOISE ESTIMATIONS

FWH formulation was used for estimating acoustic noise based on flow fields computed. The acoustic noise was captured at three receiver locations at a distance of 1m each as shown in Fig. 2. The noise at these three receiver locations was captured for the four propeller speeds. The signals collected by the three receivers in each of the four cases are shown in the Fig. 7 to 10. The time v/s pressure graph obtained is converted into frequency v/s sound pressure level plot, using Fast Fourier Transform. From the frequency v/s sound pressure level plot, it is evident that the frequency range is directly dependent on the step size chosen for the simulation.

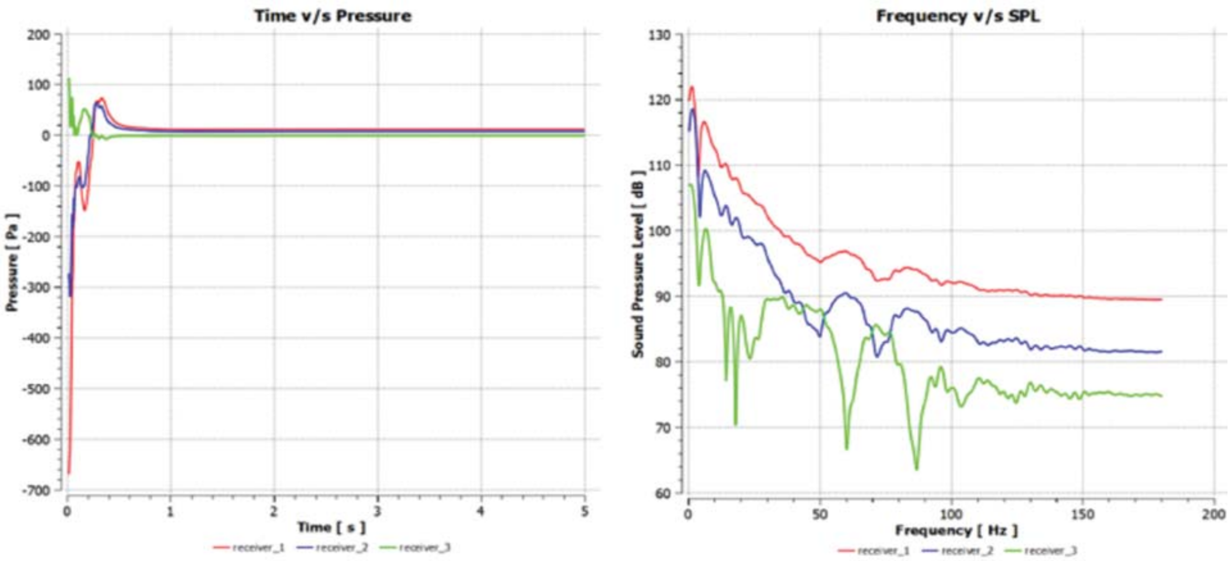

Fig. 7. Time v/s Pressure and Frequency v/s SPL graphs of case 1.

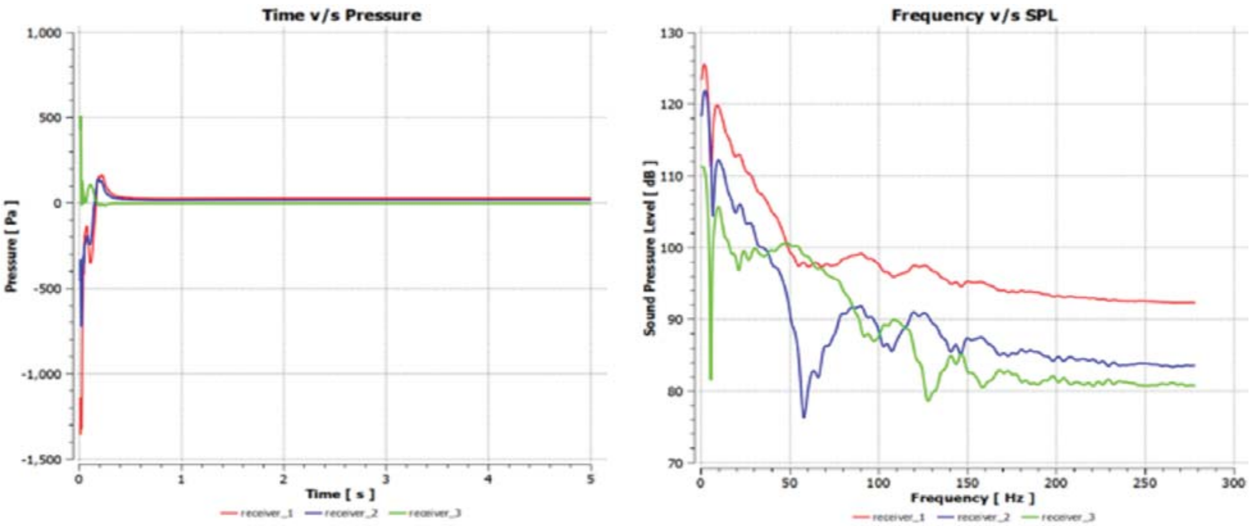

Fig. 8. Time v/s Pressure and Frequency v/s SPL graphs of case 2.

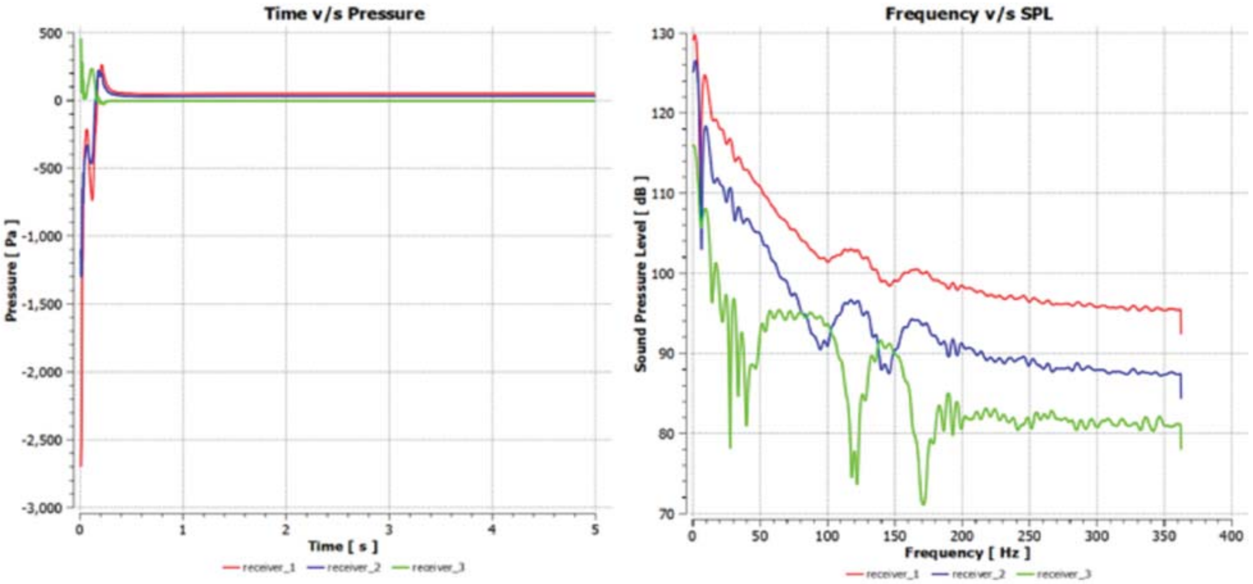

Fig. 9. Time v/s Pressure and Frequency v/s SPL graphs of case 3.

Acoustic noise so captured is also represented for all four cases at receivers 1, 2 and 3 in Fig.11 to 13.

6. *OASPL*

Overall Sound Pressure Levels can be obtained using the Equation (6). In this equation, PRMS is computed from pressure values received at the three receiver positions.

$$OASPL_{CFD} = 10 \log \left(\frac{P_{RMS}}{\mathrm{P}_{ref}}\right)^2 \tag{6}$$

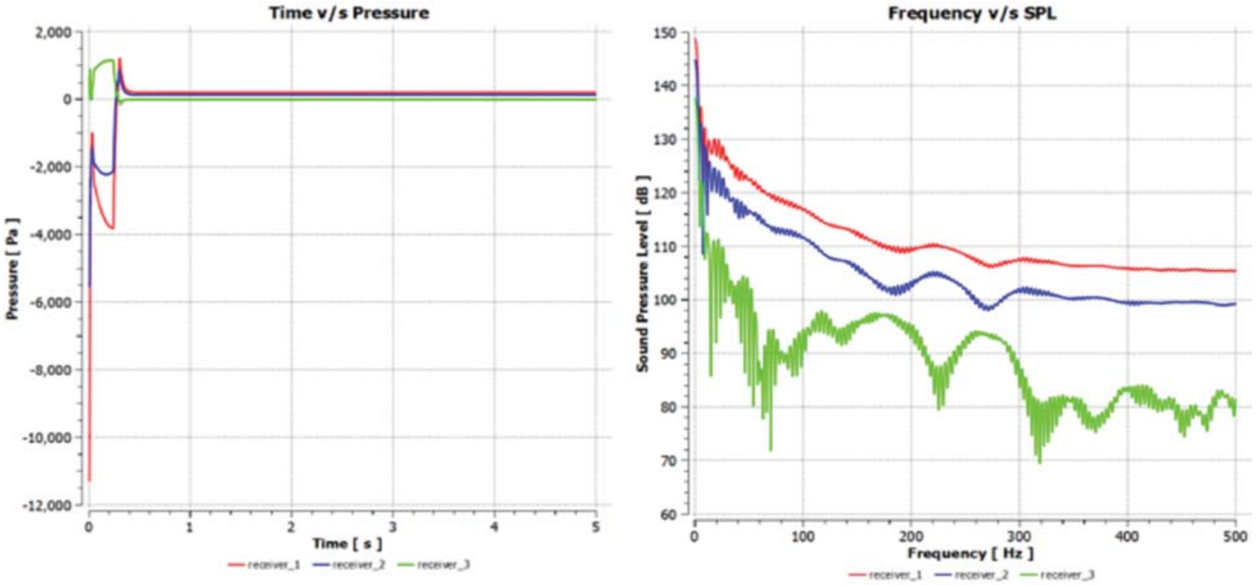

Fig. 10. Time v/s Pressure and Frequency v/s SPL graphs of case 4.

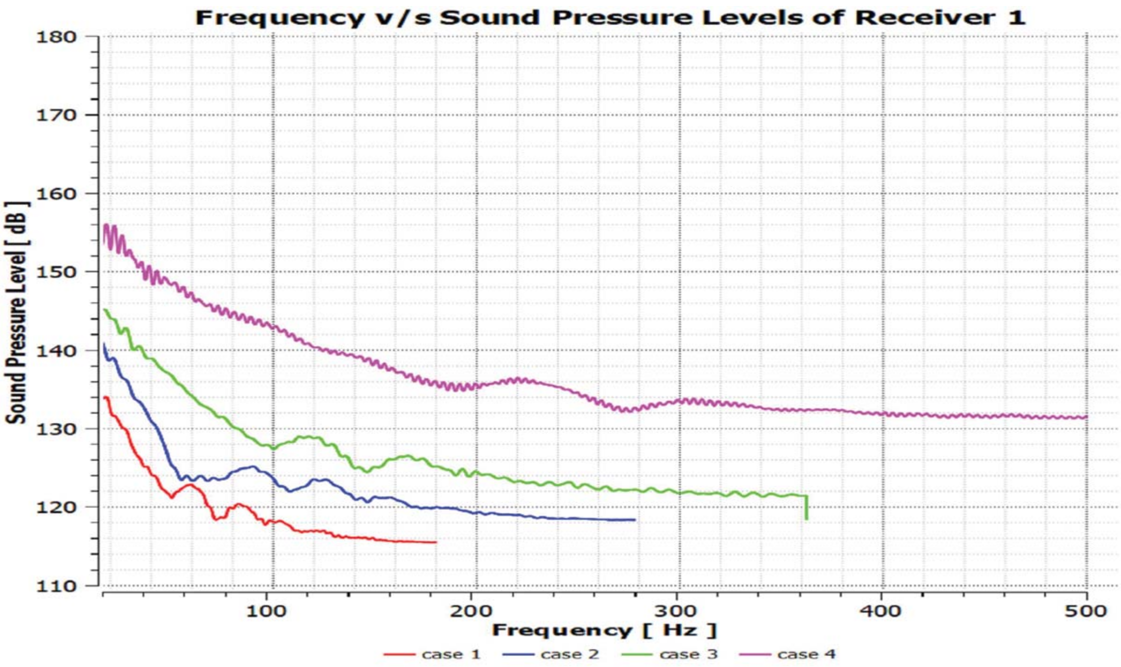

Fig. 11. Frequency v/s Sound Pressure Levels at Receiver 1.

Table 4 sums up pressures at receiver locations and provides OASPLs obtained through R_{ANS} (C_{FD}) approach.

Overall Sound Pressure Levels can also be obtained using semi-empirical formula of Equation (7).

$$OASPL_{4119} = 20 \log(n^{-9.0286} V^{4.1401} D^{-15.2608} Z^{-0.4904} T^{2.8419} Q^{0.3280}) \quad (7)$$

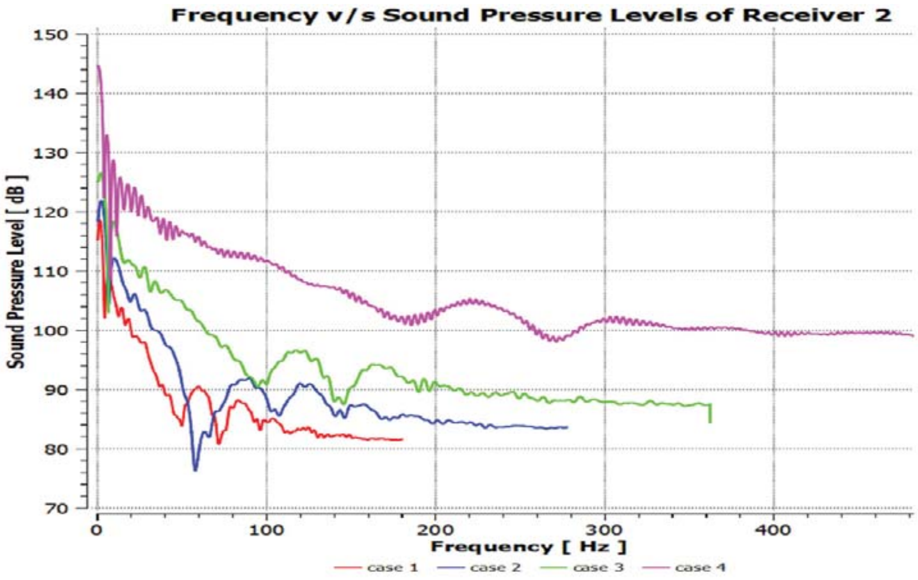

Fig. 12. Frequency v/s Sound Pressure Levels at Receiver 2.

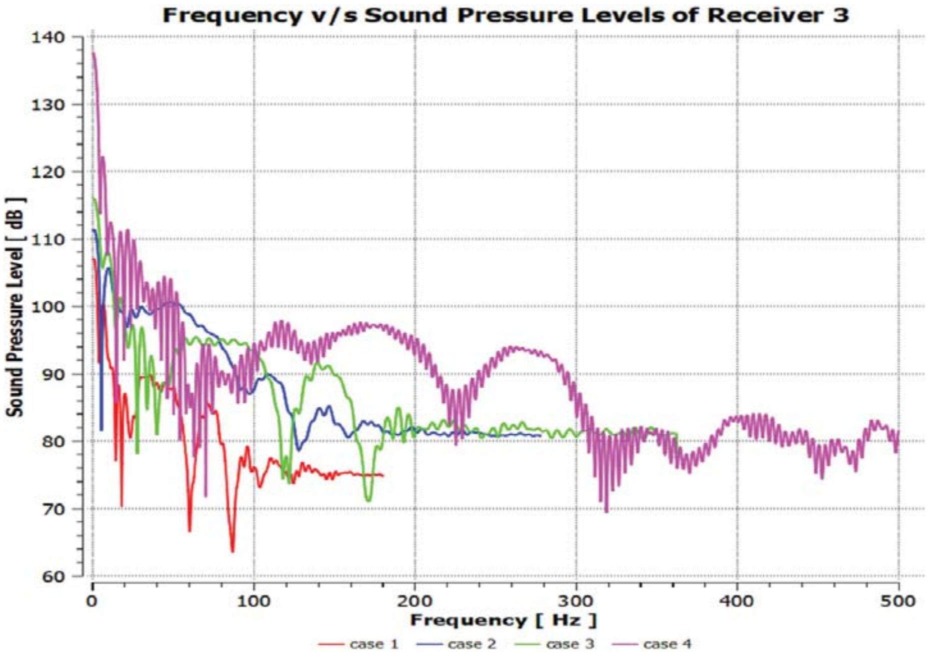

Fig. 13. Frequency v/s Sound Pressure Levels at Receiver 3.

Table 4. OASPL based on CFD (URANS) approach.

V (m/s)	P1 (1, 0, 0)	P2 (0.7, 0.7, 0)	P3 (0, 1, 0)	PRMS	OASPL (URANS)
2.539	12	8	-1	14.456	143.201
3.808	27	18	-2	32.511	150.240
5.078	50	32	-3	59.439	155.481
10.156	200	130	-13	238.891	167.564

Where,

n is propeller RPS, V is inlet velocity, D is diameter of the propeller, Z is number of blades, T is thrust of propeller and Q is propeller moment

Using this equation, OASPLs computed for the given conditions for DTMB 4119 propeller are tabulated in Table 5.

Table 5. OASPL based on semi-empirical relation.

S. No.	n	v	T	Q	OASPL (SEMI-EMP)
1	10	2.539	124.059	6.903	130.244
2	15	3.808	280.305	15.443	135.437
3	20	5.078	499.530	27.370	139.119
4	40	10.156	2005.674	148.813	148.825

7. RESULTS AND DISCUSSION

From the results, following inferences are drawn:

- It is seen that OASPLs computed using URANS based CFD are higher by about 10 to 20 dB compared to those using Semi-empirical formula.
- It is also seen that the difference in OASPL between the two methods is higher for higher propeller speed.
- The difference in OASPLs is attributable to the limitation of the RANS turbulence model whereas LES or DNS would have been expectedly more accurate. However, computational effort and time are the main constraints for using LES or DNS.

8. CONCLUSION

A comprehensive hydro-acoustic investigation was performed, employing the unsteady RANS along with the Ffowcs-Williams and Hawkings (FW-H) equation. This combination of computational fluid dynamics (CFD) and acoustic modelling was instrumental in understanding the acoustic characteristics of a propeller operating at varying velocities and rotation speeds. However, the analysis also highlighted the limitations of the URANS-FW-H approach as the prediction is seen to provide over estimate of noise levels though the trend of noise with varyng propeller speed is captured correctly. It would therefore be prudent to adopt LES or DNS along with FWH for capturing noise levels more accurately.

REFERENCES

[1] Soydan, Ahmet, Zafer, Baha, Bal and Sakir, 2019. Investigation of underwater noise characteristics of DTMB4119 propeller under different conditions, *10th Ankara International Aerospace Conference.*

[2] Esteves, Fillipe, Gomes, Gustavo, Katsuno, Eduardo, Dantas and João, 2018. Simulation of DARPA sub off model propeller-hull interaction, *27th International Congress on Waterway Transport, Naval and Offshore Construction.*

[3] M. Cansın Özden, Ahmet Y. Gürkan, Yasemin Arıkan Özden, Talat G. Canyurt and Emin Korkut, 2016. Underwater radiated noise prediction for a submarine propeller in different flow conditions, *Ocean Engineering*, **126,** 488-500.

[4] Mousavi B., Rahrovi A. and Kheradmand S., 2014. Numerical simulation of tonal and broadband hydrodynamic noises of non-cavitating underwater propeller, *Polish Maritime Research*, **21**(3), 46-53.

[5] Gaggero, S., Villa, D. and Brizzolara, S., 2010. RANS and panel method for unsteady flow propeller analysis. *Journal of Hydrodynamics, Ser. B,* **22**(5), 564-569.

The Journal of Acoustical Society of India : Vol. 52, No. 1, 2025 (pp. 11-17)

Coupled natural frequencies of a water-loaded unbaffled plate

Hemanta Dikshit[1*] and Venkata R. Sonti[2]

Department of Mechanical Engineering, Indian Institute of Science, Bengaluru-560 012, India
e-mail: hemantad@iisc.ac.in

[Received: 30-07-2025; Accepted: 22-08-2025]

ABSTRACT

This paper presents a closed form expression for the coupled natural frequencies of a simply-supported rectangular unbaffled water loaded plate. The Kirchhoff-Helmholtz Integral Equation is used to define the radiated sound pressure at any arbitrary point in the surrounding fluid medium in terms of the acoustic pressure difference across the plate and the gradient of the Green's function. Using Euler's equation and the definition of the Green's function in the wavenumber domain, the coupled equation of motion is obtained for the solution of the plate displacement. This coupled equation carries a term called the modal coupling coefficient, which describes how the vibration of one plate in vacuo mode interacts with another mode in the presence of heavy fluid loading. The improper double integral in the coupling coefficient is computed in a closed form using branch cuts in the complex plane and by making approximations. This closed form solution includes a residue term arising from the integral in the complex plane and other terms. By considering this residue term in the solution of the coupling coefficient, a small fluid loading parameter is introduced into the coupled equation of motion for the free vibration problem. Subsequently, with the help of the fluid loading parameter, singular perturbation technique is used to derive a closed form expression for the coupled natural frequencies. The accuracy of this closed form expression is validated by comparison with simulation results.

1. INTRODUCTION

The heavy fluid loading significantly changes the natural frequency of a vibrating structure compared to those in a vacuum. In this paper, a closed form expression for the coupled natural frequencies of a simply-supported unbaffled plate is derived using the singular perturbation method. Pope and Leibowitz[1] presented analytical expressions for the modal coupling coefficient of a baffled plate. For the unbaffled plate, analytical expression of the self-modal coupling coefficient is derived for corner-corner modal interaction. Subsequently, the residual contribution of this expression is used to derive the closed form solution for coupled resonances.

2. THE COUPLED EQUATION OF MOTION

Consider a flexible thin rectangular unbaffled plate ($0 \leq x \leq a$, $0 \leq y \leq b$)of area S_p, lying in the plane $z = 0$ and submerged in water, which has a characteristic impedance of ρ_0 c. The plate is excited by a point harmonic force $\tilde{\mathrm{F}}\,e^{-j\omega t}$ at the point (x_e, y_e). The resulting flexural vibrations of the plate generate acoustic pressure waves in the surrounding fluid medium, represented by p^+ (x, y, z, t) and p^- (x, y, z, t) in the $z > 0$ and $z < 0$ regions, respectively. The time dependence factor ($e^{-j\omega t}$) is omitted from further derivations. The coupled equation of motion for the plate (at the z = 0 plane) can be written as

$$D\nabla^4 W(x, y) - \overline{m}\,\omega^2 W(x, y) = F(x, y) + \Delta p(x, y, z = 0) \tag{1}$$

where $D = \dfrac{Eh^3}{12(1-\mu^2)}$ is the bending stiffness of the plate, W(x, y) is the plate displacement, $\overline{m}$ is the mass per unit area of the plate and F(x, y) is the external force. The term $\Delta p(x, y, z = 0) = p^-(x, y, z = 0) - p^+(x, y, z = 0)$ represents the acoustic pressure difference between the upper and lower surfaces of the plate. The displacement W(x, y) for a simply-supported plate is given by

$$W(x, y) = \sum_{m,n=1}^{\infty} B_{mn}\, \phi_{mn}(x, y) \tag{2}$$

where B_{mn} is the modal displacement amplitude and $\phi_{mn}(x, y) = \sin\left(\dfrac{m\,\pi\,x}{a}\right)\sin\left(\dfrac{n\,\pi\,y}{b}\right)$. The external force F(x, y) can also be expressed as a modal summation similar to the plate displacement as

$$F(x, y) = \sum_{m,n=1}^{\infty} F_{mn}\, \phi_{mn}(x, y) \tag{3}$$

where F_{mn} is the modal force amplitude and is given by $F_{mn} = \dfrac{4\tilde{F}}{ab}\,\phi_{mn}(x_e, y_e)$. By applying the Kirchhoff-Helmholtz integral equation to both the upper (S_{p+}) and the lower (S_{p-}) surfaces of the plate, the sound pressure at a point $M_0(x_0, y_0, z_0)$ within the $z > 0$ region can be expressed as[2]

$$p(M_0) = -\int_{S_p} \{D\nabla^4 W(x, y) - \overline{m}\omega^2 W(x, y) - F(x, y)\}\,\frac{\partial G(M, M_0)}{\partial z_M}\,dS_p \tag{4}$$

where M(x, y, z) is a point on the surface of the plate and $G(M, M_0)$ is the free space Green function. After substituting Eqs. (2) and (3) into the above equation and then applying the Euler equation, we obtain

$$\rho_0\omega^2 \sum_{m,n=1}^{\infty} B_{mn}\phi_{mn}(x_0, y_0) = -\sum_{m,n=1}^{\infty} \{\overline{m}(\omega_{mn}^2 - \omega^2)B_{mn} - F_{mn}\}\int_{S_p} \phi_{mn}(x,y)\,\frac{\partial^2 G(M, M_0)}{\partial z_M \partial z_{M_0}}\,dS_p \tag{5}$$

where $\omega_{mn} = \sqrt{D/\overline{m}}\left\{\left(\dfrac{m\pi}{a}\right)^2 + \left(\dfrac{m\pi}{b}\right)^2\right\}$ is the *in vacuo* natural frequency of mode *(m,n)*. Multiplying both sides of the above equation by $\phi_{pq}(x_0, y_0)$ and integrating over the plate area yields

$$\left(\overline{m}j\Theta(\boldsymbol{A} - \boldsymbol{I}\omega^2) + \rho_0\omega^2\frac{ab}{4}\boldsymbol{I}\right)\boldsymbol{B} = \Theta\boldsymbol{F} \tag{6}$$

where $\boldsymbol{I}$ is the matrix with elements $\boldsymbol{I}_{pqmn}$, I is the identity matrix, $\boldsymbol{B}$ is the vector containing all B_{mn} elements, $\boldsymbol{F}$ is the vector of F_{mn} and $\boldsymbol{A}$ is a diagonal matrix of squared *in vacuo* natural frequencies. $\boldsymbol{I}_{pqmn}$ is the modal coupling coefficient given by

$$\Theta_{pqmn} = \frac{1}{8\pi^2}\int_{-\infty}^{\infty}\int_{-\infty}^{\infty} \kappa_Z \Phi_{pq}(-\lambda, -\mu)\,\Phi_{mn}(\lambda, \mu)\,d\lambda d\mu.$$

For the admissible function given in Eq. (2)

$$\Phi_{mn}(\lambda, \mu) = \frac{(m\pi/a)[(-1)^m e^{i\lambda a} - 1]}{[\lambda^2 - (m\pi/a)^2]}\;\frac{(n\pi/b)[(-1)^n e^{i\lambda b} - 1]}{[\mu^2 - (n\pi/b)^2]} \tag{7}$$

2.1 The Modal Coupling Coefficient

The real part of the Θ_{pqmn} represents radiation damping, whereas the imaginary part contributes to coupled natural frequencies. The Θ_{pqmn} is non-zero only when p + m and q + n are both even. These nonzero values of Θ_{pqmn} are given by

$$\Theta_{pqmn} = \frac{4k_p k_q k_m k_n}{8\pi^2} \mathrm{I}^{\mathrm{pqmn}} \tag{8}$$

where

$$I^{pqmn} = \int_{-\infty}^{\infty}\int_{-\infty}^{\infty} \frac{[1-(-1)^p \cos\lambda \mathrm{a}]\,[1-(-1)^{\mathrm{q}} \cos\mu \mathrm{b}]\,(\mathrm{k}^2-\lambda^2-\mu^2)^{1/2}}{(\lambda^2-\mathrm{k}_p^2)\,(\lambda^2-\mathrm{k}_m^2)\,(\mu^2-\mathrm{k}_q^2)\,(\mu^2-\mathrm{k}_n^2)}\,\mathrm{d}\lambda \mathrm{d}\mu. \tag{9}$$

where $k_p = p\pi/a$, $k_m = m\pi/a$, $k_q = q\pi/b$ and $k_n = n\pi/b$ are the *in vacuo* plate wavenumbers. In the equation above, the integral over λ is denoted as

$$I_1^{pm}(\mu) = \int_{-\infty}^{\infty} \frac{[1-(-1)^p \cos\lambda \mathrm{a}]\,(\mathrm{k}^2-\lambda^2-\mu^2)^{1/2}}{(\lambda^2-\mathrm{k}_p^2)\,(\lambda^2-\mathrm{k}_m^2)}\,\mathrm{d}\lambda. \tag{10}$$

The integrand of $I_1^{pm}(\mu)$ (Eq. 10) has square root branch points at $\lambda_{1,2} = \pm\sqrt{(\mathrm{k}^2-\mu^2)}$. Depending on the value of μ and the location of these branch points, $I_1^{pm}(\mu)$ has to be evaluated differently in two cases: when $|\mu| < k$, where the branch points $\lambda_{1,2} = \sqrt{(\mathrm{k}^2-\mu^2)}$ lie on the positive and the negative real axes and when $|\mu| > k$, where the branch points $\lambda_{1,2} = \pm \mathrm{j}\sqrt{(\mu^2-k^2)}$ lie on the positive and the negative imaginary axes. $\mathrm{I}^{\mathrm{pqmn}}$ integral (Eq. 9) can be written as

$$I^{pqmn} = 2\int_0^k \frac{[1-(-1)^q \cos\mu \mathrm{b}]}{(\mu^2-\mathrm{k}_q^2)\,(\mu^2-\mathrm{k}_n^2)} I_1^{pm}(\mu : |\mathrm{u}| < \mathrm{k})\,\mathrm{d}\mu + 2\int_k^{\infty} \frac{[1-(-1)^q \cos\mu \mathrm{b}]}{(\mu^2-\mathrm{k}_q^2)\,(\mu^2-\mathrm{k}_n^2)} I_1^{pm}(\mu : |\mathrm{u}| > \mathrm{k})\,\mathrm{d}\mu \tag{11}$$

Fahy and Gardonio[3] state that for the case of a finite panel interacting with an infinite fluid, "the structural mode shapes remain almost unchanged". This implies that the cross modal coupling due to the fluid loading is negligible and the self modal coupling terms Θ_{pqpq} are adequate. Therefore, considering only the diagonal terms of the **Θ** matrix, Eq. (6) for the free vibration problem can be written as

$$\mathrm{j}\left\{\overline{\mathrm{m}}(\omega_{pq}^2-\omega^2)\right\} + \frac{\rho_0 \omega^2 \mathrm{ab}}{4\mathrm{j}\,\mathrm{Im}\{\Theta_{\mathrm{pqpq}}\}} = 0 \tag{12}$$

In the next section, an analytical expression is derived for the imaginary part of the self-modal coupling coefficient (i.e., p = m and q = n) for corner-corner modal interaction.

2.2 Derivation of Θ_{pqpq} for corner-corner modes ($k_p > k$ and $k_q > k$)

Using the Kraichnan assumption[4,5] in Eq. (11) and knowing that $k_q > k$, the imaginary part of I_{pqpq} is given by

$$I_{\chi}^{pqpq} \approx \frac{\pi b}{2k_q^2} \mathrm{Im}[I_1^{pp}(k_q : |k_q| > k)] \tag{13}$$

where $\mathrm{Im}[I_1^{pp}(k_q : |k_q| > k)]$ denotes the imaginary part of the $I_1^{pp}(k_q : |k_q| > k)$. Fig. 1 shows the poles, branch points, branch cuts and the integration contour for $I_1^{pp}(k_q : |k_q| > k)$.

Now, using the Cauchy residue theorem we get

$$I_1^{pp}(k_q : |k_q| > k) = \pi \mathrm{j}[\mathrm{Res}(k_p) + \mathrm{Res}(-k_p)] - (\Gamma_1 + \Gamma_2) \tag{14}$$

where

$$\mathrm{Res}(-k_p) = \mathrm{Res}(\mathrm{k}_\mathrm{p}) = \frac{a\left|k^2-k_q^2-k_p^2\right|^{1/2}}{4k_p^2} \text{ and } \Gamma_1 = \Gamma_2 = \mathrm{j}\int_{\sqrt{k_q^2-k^2}}^{\infty} \frac{[1-(-1)^p e^{-ay}]\left|k_q^2-k^2-y^2\right|^{1/2}}{(y^2+k_p^2)(y^2+k_p^2)}\,\mathrm{dy}$$

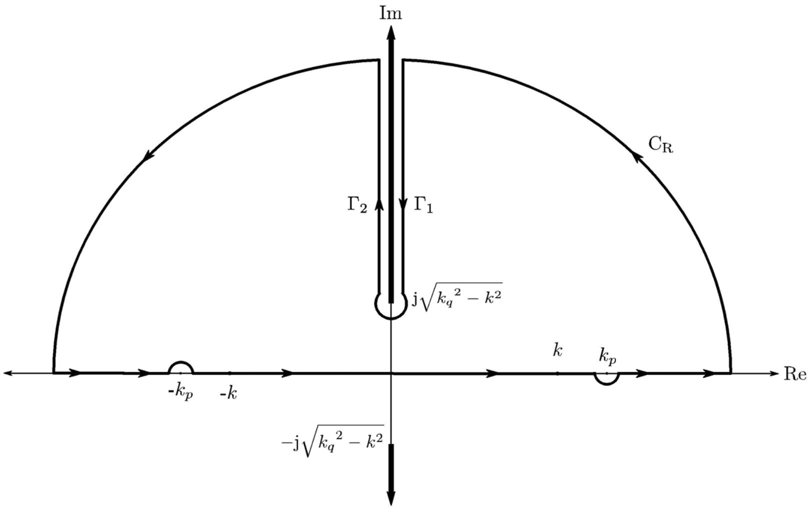

Fig. 1. Integration contour of $I_1^{pp}(k_q : \left|k_q\right| > k)$

Substituting the above equation into Eq. (13) we get

$$I_\chi^{pqpq} \approx \left[\frac{\pi^2 ab\sqrt{k_p^2+k_q^2-k^2}}{4k_p^2k_q^2} - \frac{\pi b}{k_q^2}\left\{ \frac{(k_q^2-k^2)\,\log\left(\dfrac{\sqrt{k_p^2+k_q^2-k^2}-k_p}{\sqrt{k_p^2+k_q^2-k^2}+k_p}\right) + 2k_p\sqrt{k_p^2+k_q^2-k^2}}{4k_p^3\sqrt{k_p^2+k_q^2-k^2}} \right\} \right]$$

However, the above expression is found to be a poor approximation when $k_p = k_m$ and $k_q = k_n$. A correction term, similar to the second term inside the square bracket is added to the above expression[1]. Thus, I_χ^{pqpq} is given by

$$\begin{aligned} I_\chi^{pqpq} \approx & \left[\frac{\pi^2 ab\sqrt{k_p^2+k_q^2-k^2}}{4k_p^2k_q^2} \right. \\ & - \frac{\pi b}{k_q^2}\left\{ \frac{(k_q^2-k^2)\,\log\left(\dfrac{\sqrt{k_p^2+k_q^2-k^2}-k_p}{\sqrt{k_p^2+k_q^2-k^2}+k_p}\right) + 2k_p\sqrt{k_p^2+k_q^2-k^2}}{4k_p^3\sqrt{k_p^2+k_q^2-k^2}} \right\} \\ & \left. - \frac{\pi a}{k_q^2}\left\{ \frac{(k_p^2-k^2)\,\log\left(\dfrac{\sqrt{k_p^2+k_q^2-k^2}-k_p}{\sqrt{k_p^2+k_q^2-k^2}+k_p}\right) + 2k_p\sqrt{k_p^2+k_q^2-k^2}}{4k_p^3\sqrt{k_p^2+k_q^2-k^2}} \right\} \right] \end{aligned} \qquad (15)$$

The imaginary part of the modal coupling coefficient Θ_{pqpq} is evaluated using Eq. (8).

2.3 Closed form expression for coupled natural frequency

The analytical expression for I_{χ}^{pqpq} has a residue contribution and some other extra terms as shown in Eq. (15). The entire I_{χ}^{pqpq} as a residue contribution multiplied by a factor 1/β, is represented as shown below

$$\frac{1}{\beta}\ \frac{\pi^2 ab\sqrt{k_p^2+k_q^2-k^2}}{4k_p^2k_q^2} = \left\{\int_{-\infty}^{\infty}\int_{-\infty}^{\infty}\frac{[1-(-1)^p\ \cos\lambda a][1-(-1)^q\ \cos\mu b](k^2-\lambda^2-\mu^2)^{1/2}}{(\lambda^2-k_p^2)\ (\mu^2-k_q^2)^2}\mathrm{d}\lambda\mathrm{d}\mu\right\} \tag{16}$$

Fig. 2 shows the variation of the beta factor for mode (1,1) of a steel plate (a = 0.455 m, b = 0.546 m and h = 0.006 m) in a water medium (ρ_0 = 998.2 kg/m^3 and c = 1481 m/s). The material parameters are: E = 200 GPa, ρ_p = 7850 kg/m^3 and ν = 0.30. The values of the β factor are calculated by numerically computing the right hand side of Eq. (16), using the speed of sound in the water medium. The value of k is varied corresponding to ω ranging from the coupled frequency to the in vacuo frequency of the (1,1) mode.

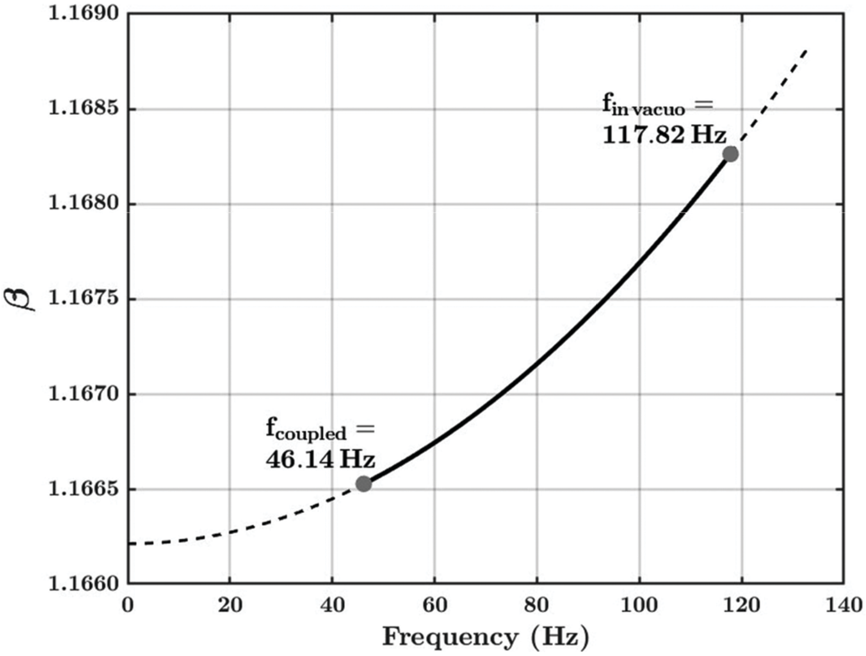

Fig. 2. Variation of β factor for mode (1,1) with frequency.

It can be seen that the value of β is largely insensitive to the frequencies in this range. The coupled resonance frequency value of 46.14 Hz is obtained from Eq. (12) by numerically integrating the Θ_{pqpq}. As β is insensitive to a range of frequencies, it is computed from Eq. (16) at the in vacuo frequency of the *(p, q)*th mode using the analytical expression of the double integral (Eq. 15). Only for the plotting of Fig. 2 the numerical integration was used to calculate the values of β.

After finding β, substituting Eqs. (8), (9) and (16) into Eq. (12) to obtain

$$(\alpha^4-\omega^2)\sqrt{\alpha^2\omega_g-\omega^2}-2\beta\varepsilon\omega_g\omega^2=0 \tag{17}$$

where $\alpha\sqrt{\omega_{pq}}$, ω_{pq} is the *in vacuo* frequency of the (p, q)th mode, $\omega_g = c^2\sqrt{\frac{\rho_p h}{D}}$ coincidence frequency and $\varepsilon = \frac{\rho_0{}^c}{\bar{m}\omega_g}$ is the intrinsic fluid-loading parameter[6]. Then the Eq. (17) is solved for the coupled natural frequency ω using the singular perturbation method by substituting $\alpha = \frac{N}{\varepsilon^2}$ into the equation, where N is an O(1) quantity. After substitution, some terms within the equation have higher order values of ω_g, which for the steel and water properties mentioned above is 2.39 × 10^5 rad/sec. These higher order terms nullify the effect of the small parameter ε in the asymptotic expansion; hence, ω_g is replaced with $\frac{\omega'_g}{\varepsilon^6}$ to obtain

$$\mathrm{N}^{10}\omega'_g - N^8\omega^2\varepsilon^{10} - 2N^6\omega^2\omega'_g\varepsilon^8 - (4\beta^2\omega'^2_g - N^2\omega'_g)\varepsilon^{16}\omega^4 + 2N^4\omega^4\varepsilon^{18} - \omega^6\varepsilon^{26} = 0 \tag{18}$$

Next, variable ω is scaled using the transformed variable y as

$$\omega = y\frac{N^2}{\sqrt{2}\varepsilon^4} \tag{19}$$

Substituting the above equation into Eq. (18) yields

$$N^2\omega'_g - 0.5N^4y^2\varepsilon^2 - N^2y^2\omega'_g - (\beta^2\omega'^2_g - 0.25N^2\omega'_g)y^4 + 0.5N^4y^4\varepsilon^2 + 0.125y^6N^4\varepsilon^2 = 0 \tag{20}$$

The unperturbed roots as $\varepsilon \to 0$ are

$$y_{0_{(1,2)}} = \pm\left(\frac{\sqrt{2}\sqrt{(N^2 - 4\beta^2\omega'_g)(N - 2\beta\sqrt{\omega'_g})N}}{N^2 - 4\beta^2\omega'_g}\right) \text{ and } y_{0_{(3,4)}} = \pm\left(\frac{\sqrt{2}\sqrt{(N^2 - 4\beta^2\omega'_g)(N + 2\beta\sqrt{\omega'_g})N}}{N^2 - 4\beta^2\omega'_g}\right)$$

For specific values of N and β, $y_{0(3,4)}$ becomes complex. Since ω cannot be both complex and negative, the positive value of $y_{0(1,2)}$ is selected as the unperturbed root. Subsequently, substituting $y = y_0 + y_1\varepsilon^2 + y_2\varepsilon^4$ into the Eq. (20) and expanding about $\varepsilon = 0$, we obtain

$$\begin{aligned} y = &\{(-0.5y_0^2 + 0.5_0^4 - 0.125y_0^6)N^4 + (-2\omega'_g y_0 y_1 + y_0^3 y_1 w'_g)N^2 - 4y_0^3 y_1 \beta^2\omega'^2_g\} \\ &\varepsilon^2 + \{(-y_0y_1 + 2y_0^3y_1 - 0.75y_0^5y_1)N^4 + (-\omega'_g(2y_0y_2 + y_1^2) + (y_0^3y_2 + 1.5y_0^2y_1^2)\omega'_g)N^2 - (4y_0^3y_2 + 6y_0^2y_1^2)\beta^2\omega'^2_g\}\varepsilon^4 \end{aligned} \tag{21}$$

By equating the coefficients of ε^2 and ε^4 in the Eq. (21), we get

$$y_1 = \frac{0.125y_0(y_0^4 - 4y_0^2 + 4)N^4}{\omega'_g(-4\beta^2y_0^2\omega'_g + N^2y_0^2 - 2N^2)} \text{ and } y_2 = \frac{0.0078y_0N^8}{\omega'^2_g(-4\beta^2y_0^2\omega'_g + N^2y_0^2 - 2N^2)}\{(y_0^4 - 4y_0^2 + 4)$$
$$(-36\beta^2y_0^6\omega'_g + 9N^2y_0^6 + 80\beta^2y_0^4\omega'_g - 42N^4y_0^4 - 16\beta^2y_0^2\omega'_g + 60N^2y_0^2 - 60N^2y_0^2 - 24N^2)\}$$

Substituting the values of y_0, y_1 and y_2 into the expression for y ($y_0 + y_1\varepsilon^2 + y_2\varepsilon^4$) and then using the Eq. (19) , the coupled natural frequency ω can be expressed as

$$\omega = \frac{(y_0 + y_1\varepsilon^2 + y_2\varepsilon^4)N^2}{\sqrt{2}\varepsilon^4} \tag{22}$$

3. RESULTS AND DISCUSSION

In this section, the coupled natural frequencies of a water-loaded plate are computed using the closed form expression presented in this work. The plate and water properties are the same as in section 4. Table 1 compares the coupled natural frequency values obtained from the Eq. (22) with those obtained by numerically integrating the Θ_{pqpq} in Eq. (12). To ensure that the coupled natural frequency values obtained using Eq. (22) are within a reasonable range, the numerical simulations were done using the commercial software LMS Virtual Lab.

To keep the article brief, the analytical expression of the modal coupling coefficient was presented only for corner-corner modal interactions. The coupled natural frequencies of the corner modes are shown in Table 1. The coupled natural frequencies obtained from the closed form expression show a maximum

Table 1. Coupled resonance frequencies (for corner modes) of a water-loaded plate calculated using Eq. 22 and from LMS Virtual Lab. In the numerical solution of Eq. 12, Θ_{pqpq} is obtained by numerical integration.

Mode	Closed form Eq. 22 (Hz)	LMS (Hz)	Numerical solution Eq. 12 (Hz)
(1,1)	46.92	45.55	46.14
(1,2)	125.10	123.59	124.63
(2,4)	645.51	642.93	645.20
(5,5)	2089.68	2088.45	2089.73
(7,5)	3440.00	3441.18	3441.07
(8,11)	8226.89	8237.16	8229.47

error of 2% for the (1,1) mode compared to the numerical solutions across all modes (corner and edge modes) within the 10 kHz frequency range.

REFERENCES

[1] L.D. Pope and R.C. Leibowitz, 1974. Intermodal coupling coefficients for a fluid-loaded rectangular plate, *J. Acoust. Soc. Am.*, **56**(2), 408-415.

[2] B. Laulagnet, 1998. Sound radiation by a simply supported unbaffled plate, *J. Acoust. Soc. Am.*, **103**(5), 2451-2462.

[3] F. Fahy and P. Gardonio, 2007. *Sound and Structural Vibration - Radiation, Transmission and Response*, Academic Press, UK.

[4] H.G. Davies, 1971. Low frequency random excitation of water-loaded rectangular plates, *J. Sound Vib.*, **15**(1), 107-126.

[5] R.H. Kraichnan, 1957. Noise transmission from boundary layer pressure fluctuations, *J. Acoust. Soc. Am.*, **29**(1), 65-80.

[6] D.G. Crighton, 1989. The 1988 rayleigh medal lecture: Fluid loading - the interaction between sound and vibration, *J. Sound Vib.*, **133**(1), 1-27.

The Journal of Acoustical Society of India : Vol. 52, No. 1, 2025 (pp. 18-24)

Vibration analysis of structural members with effect of piezoelectric smart materials

K. Meera Saheb and S. Khaja Basha*
Department of Mechanical Engineering, University College of Engineering (A),
Jawaharlal Nehru Technological University, Kakinada-533 003, India
e-mail: basha365shaik@gmail.com

[Received: 29-07-2025; Accepted: 22-08-2025]

ABSTRACT

This study explores numerical and experimental tools to analyze the impact of vibration reaction processes on aluminum structural beams. The research endeavor focuses on how various boundary conditions affect vibration mitigation and how well PVDF (polyvinylidene fluoride) patches work. PVDF piezo sensor is employed to apply a counteracting force using a 12V electric input to reduce vibrations. This process is facilitated through a function generator, ME Scope, and Samurai software. The research emphasizes the use of active vibration control in several industries, such as Aeroplan structures, helicopter blades, cargo ships, submarines, and marine vehicles. The high degree of alignment between the numerical findings produced by ANSYS APDL 2024 R1 and experimental modal analysis validates the precision and dependability of the numerical models as well as the efficacy of the vibration control techniques used.

1. INTRODUCTION

Research on piezoelectric sensors, energy generation, and vibration controllers has been gradually expanding for decades. The effect of piezoelectric, first discovered by Pierre and Curie in the 1880s, occurs when mechanical stress is applied to some materials, causing them to produce an electrical charge. The Greek term "piezein," which indicates to force itself or squeeze, is where the phrase "piezoelectric" originates. One special characteristic of piezoelectric materials is their capacity to convert electrical energy from mechanical energy and vice versa. these materials generate mechanical vibrations when an electric charge is applied. To analyse the vibration characteristics, various boundary circumstances are applied to beams that have been prepared with adhesives to connect piezoelectric sensors.

Yashavantha Kumar and Sathish Kumar[1] investigated free vibration behavior of a smart composite cantilever beam with PZT patches. Modal shapes and fundamental frequencies are identified via ANSYS Modal Analysis, which also demonstrates how variations in these modes might be a sign of damage. The results demonstrate how useful Modal Analysis is for tracking the structural integrity of smart composite materials. Sharvari S. Heganna, *et al.*[2] brought out that piezoelectric materials can be employed as actuators to induce structural changes and vibration suppression can be achieved through their inverse piezoelectric effect. They further stated that these materials can be applied for vibration sensors and to generate the oceanic applications to harvest electrical energy and give the pre-instructions of precipitate moments of climate changes. Various methods are used in the setup consisting of three components such as an exciter (a Lead-Zirconate-Titanate patch), a sensor (a second patch that detects the disturbance in real-time) and an actuator (a third patch that dampens vibrations).

Singh, Saurav Sharma, *et al.*[3] found that the passive structure's inherent frequencies are moved to higher frequencies by the presence of patches. Modal analysis was used to establish where the actuators and piezo sensors should be placed on the beam or plate. It may detect the deformation brought on by the stimulation of the structure and be used as a sensor. It is frequently utilized as an active control of the positive piezoelectric effect of piezoelectric materials. Schlaberg, Duff, *et al.*[4] studied the Electrical and Mechanical properties of two different piezoelectric composite materials.

Li and Narita[5] studied vibration reduction in laminated cylindrical panels using piezoelectric Fiber reinforce composite material with different boundary conditions. Bendine, Boukhoulda, *et al.*[6] studied vibration suppression in composite plates by varying position of the piezoelectric patches using LQR control algorithm. Balamurugan and Narayanan[7] used C_o 9 node quadrilateral shell element shear flexible element to suppress vibrations in composite plate shell structures by bonding PZT piezo ceramic patches.

Tzou and Tseng[8] investigated distributed piezoelectric sensor / actuator systems operating in steady-state temperature fields. This work investigates piezo thermoelastic effects. The influence of thermal effects on sensing and control in piezoelectric laminates is analyzed, and a 3-D hexahedron finite element model integrating thermal, electric, and mechanical energies is formulated. Singh , Sharma, *et al.*[9] investigated he poling-tuned piezoelectric actuators for active vibration control of a smart cantilever beam. 49-rule fuzzy logic controller is put into practice. Poling tuning improves performance by turning on many piezoelectric strain coefficients. At a 53° poling angle, PMN-0.42PT exhibits a 60.78% improvement, BT-NNb a 36.75% increase, and PZT-7A a 15.53% improvement.

2. MATERIALS AND THEIR PROPERTIES

In this dynamic study, vibration response of beams made of isotropic materials added with piezo electric (PVDF) patches was studied. Focus was on extracting the natural frequency and mode shapes. In this work, various types of boundary conditions C-F, S-S, C-S, and C-C were applied.

It has been noted that for the first three modes of the smart beams, the beam with clamped-free boundary conditions displays lower natural frequencies than the other beam boundary conditions, while the beam with clamped-clamped boundary conditions displays higher natural frequencies. The different levels of flexibility connected to the end conditions are the cause of this discrepancy. This discovery implies that, in comparison to the other four beam boundary conditions, the (C-C) beam exhibits significantly higher stiffness.

3. EXPERIMENTAL WORK

Experiments were conducted using isotropic aluminum beams, each bonded with piezoelectric PVDF sensors. These samples, prepared with various beam boundary conditions, were subjected to EMA (Experimental Modal Analysis) to identify their vibration properties and dynamic qualities. A free vibration test was part of the experimental setup used for the modal analysis in order to evaluate the modal behavior. Eight input channels were employed in a data collection system (DAQ) to examine features like natural frequencies and mode shapes. Two input channels were chosen to link an impact hammer and an accelerometer out of these.

Using beeswax, the accelerometer was fastened to the beam sample, while a function generator (FG) supplied the PVDF sensors with a 12V electrical input. The accelerometer measured the vibration response by converting it into electrical signals recording the sample's reaction to vibrations at various locations across the structure. A quartz-tipped impact hammer produced an excitation shock, establishing the modal analysis's beginning input frequency and magnitude. The vibration information were processed using SAMURAI software, which extracted data from the frequency response function (FRF) curves, and post-

Table 1. Properties of PVDF.

Parameter	Value
Density	1800 kg/m^3
Elastic Stiffness Matrix	
C_{11}	12.6×10^{10} N/m^2
C_{12}	7.95×10^{10} N/m^2
C_{13}	8.41×10^{10} N/m^2
C_{33}	11.7×10^{10} N/m^2
C_{44}	2.33×10^{10} N/m^2
Piezoelectric Strain Matrix	
E_{31}	6.5 C/m^2
E_{33}	23.3 C/m^2
E_{15}	17 C/m^2
Dielectric Matrix	
ε_{11}	1.5×10^{-8} F/m
ε_{22}	1.5×10^{-8} F/m
ε_{33}	1.5×10^{-8} F/m
Properties of Aluminium	
Modulus (E)	7.1*1010 N/m^2
Density (p)	2700 kg/m^3
Poisson's Ratio (μ)	0.3

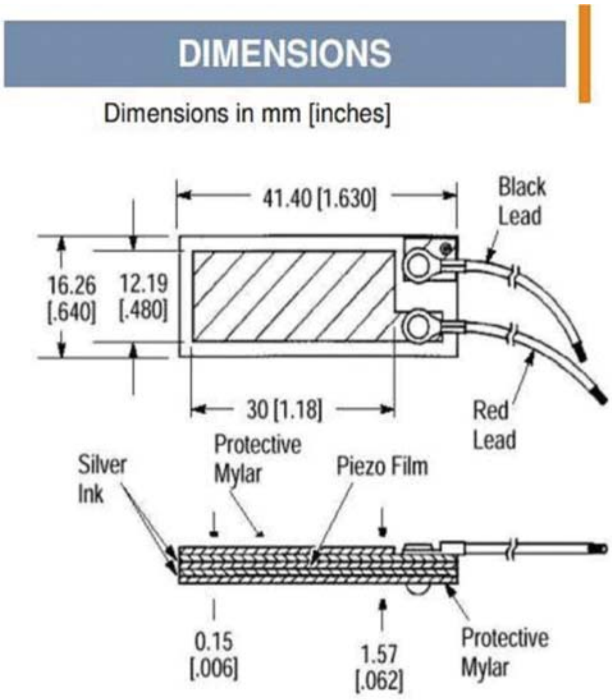

Fig. 1. PVDF patch Schematic.

processing was carried out utilizing ME' Scope program was to assess log magnitude and other important data. In order to produce an illustration of mode forms, the natural frequencies are extracted from the FRFs that were acquired from the testing and assigned to the ME Scope structure alongside the FRFs.

Smart beams are subjected to Finite Element Analysis (FEA) using the Ansys APDL 2024 R1 software. The following mechanical parameters are added to an isotropic beam model in the horizontal region, measuring 160 x 30 x 2 mm and 230 x 250 x 2 mm: modulus of elasticity •, Poisson's ratio (μ), and density

Fig. 2. Experimental Setup

Table 2. Properties of Aluminium.

Parameter	**Value**
Modulus (E)	7.1*1010 N/m^2
Density (p)	2700 kg/m^3
Poisson's Ratio (μ)	0.3

(ρ) of Aluminium as listed in Table 2. Piezoelectric sensor dimensions are 41.40 x16.26 x 0.4 mm and its properties are given in Table 1. In beam the PVDF patch is placed at 10 mm from the left end of the beam. In case of plates, four number of equal sizes PVDF patches are bonded in a quaternal area with 12V electric energy supply. Ansys 2024 R1 APDL software was used and planes are modelled as coupled field [Brick 20node 226 is used for meshing] for a piezoelectric sensor in anisotropic properties and SOLID [20 node 186] for isotropic properties and composite each of which has six degrees of freedom. Fig. 3 shows FE model of beam with PVDF patch. Fig. 4 to 7 represent beam with PVDF subject to different boundary conditions (C-F, C-C, S-S, C-S). These were used for experimental modal analysis of the beams with attached pvdf patches for the isotropic Aluminium beam.

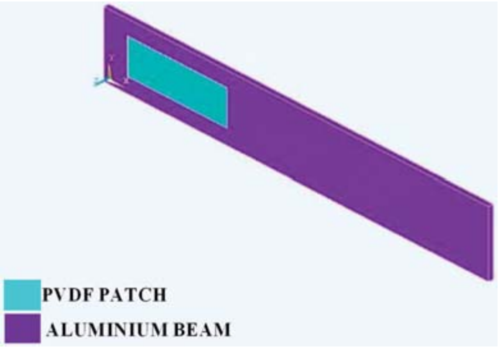

Fig. 3. A finite element mesh model of a 160x30x2 mm beam with a 41.4x16.26x0.4 (mm) PVDF patch.

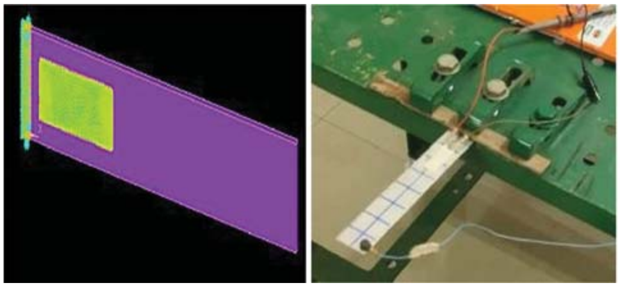

Fig. 4. A Rectangular beam with a PVDF patch, subject to a C-F boundary condition includes 12V electric supply.

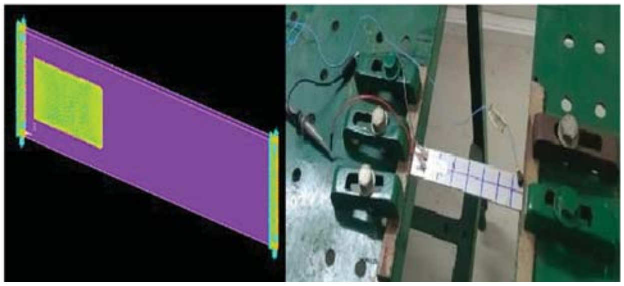

Fig. 5. A Rectangular beam with a PVDF patch, subject to a C-C boundary condition includes 12V electric supply.

Fig. 6. A Rectangular beam with a PVDF patch, subject to a C-S boundary condition includes 12V electric supply.

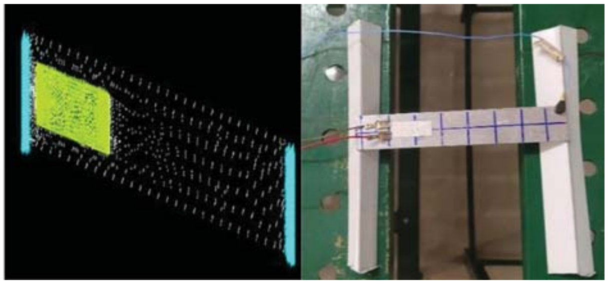

Fig. 7. A Rectangular beam with a PVDF patch, subject to a S-S boundary condition includes 12V electric supply.

4. RESULTS AND DISCUSSIONS

This section presents the results for the beams' intrinsic frequencies and mode configurations. The study emphasizes the outcomes of ANSYS APDL and Experimental Modal Analysis for an aluminum plate equipped with piezoelectric patches, examining three distinct case studies. (i) Aluminium Beam,

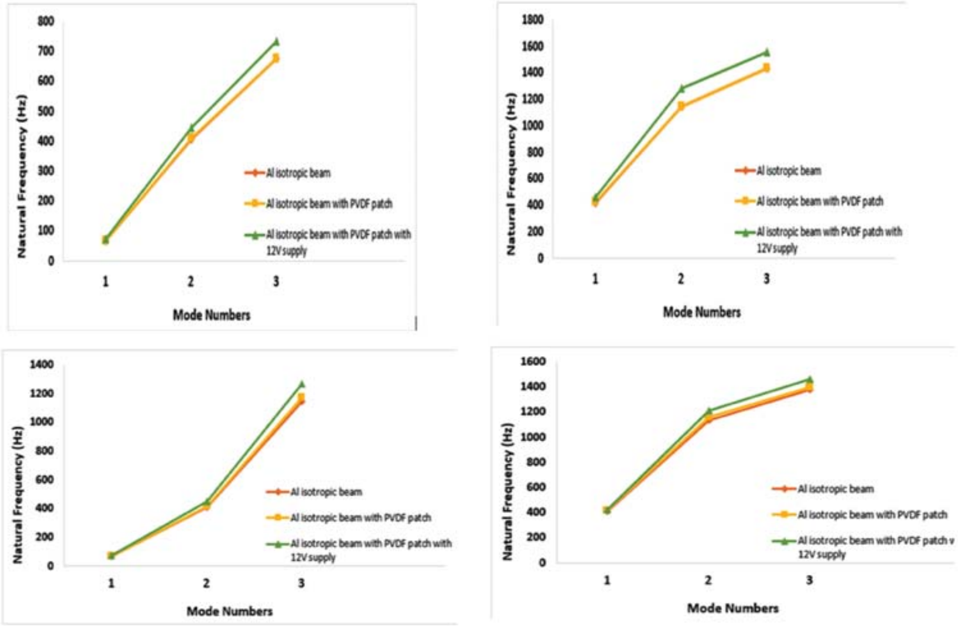

Fig. 8. Variation of natural frequencies with mode number for Aluminium beam C-F, C-C, C-S and S-S with PVDF patch and 12V energy supply.

Table 3. Natural frequencies (Hz) of an aluminum rectangular beam with piezoelectric patches under various beam boundary conditions.

Boundary condition & Mode No.		Ansys				EMA			Error (%)
		Isotropic beam (A)	Isotropic beam with PVDF patches (B)	Isotropic beam with PVDF patch with 12V (C)	Percentage difference (%) (C) and (A)	Isotropic beam (a)	Isotropic beam with PVDF patches (b)	Isotropic beam with PVDF patches with 12V (c)	(c) and (C)
C-F	1	64.985	65.909	71.420	9.011	61.900	63.100	69.400	2.823
	2	406.592	410.080	444.271	8.481	406.000	409.000	435.000	2.086
	3	676.243	674.866	731.194	7.515	674.000	675.000	732.000	0.110
C-C	1	416.358	422.193	457.390	8.971	415.000	426.000	454.000	0.741
	2	1146.06	1146.358	1280.600	10.511	1142.000	1180.000	1285.000	0.342
	3	1430.63	1430.631	1556.900	8.110	1439.000	1430.000	1560.000	0.198
C-S	1	64.986	65.9197	71.421	9.010	63.100	66.300	71.900	0.667
	2	406.621	410.151	444.343	8.489	407.000	413.000	448.000	0.816
	3	1139.62	1167.841	1264.980	9.909	1160.000	1168.000	1280.000	1.173
S-S	1	409.391	411.264	417.386	4.210	410.000	406.000	416.000	0.331
	2	1132.43	1160.821	1206.330	6.126	1133.000	1160.000	1210.000	0.303
	3	1375.74	1391.825	1459.700	5.752	1380.000	1390.000	1449.000	0.738

(ii) Aluminium Beam with Pvdf Patch and (iii) Aluminium Beam with Pvdf Patch With 12V Electrical Supply. Fig. 8 shows variation of Natural frequencies with mode number for the three configurations studies under different boundary conditions. Table 3 shows comparative results from FEA and experiments for Natural frequencies. Fig. 9 to 12 presents first three modes obtained using FEA and EMA for different boundary conditions.

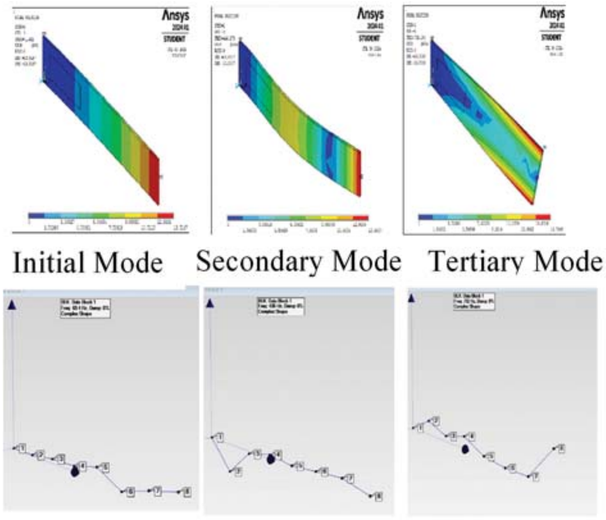

Fig. 9. First three modes of Al beam (F-F) with patch and 12V supply.

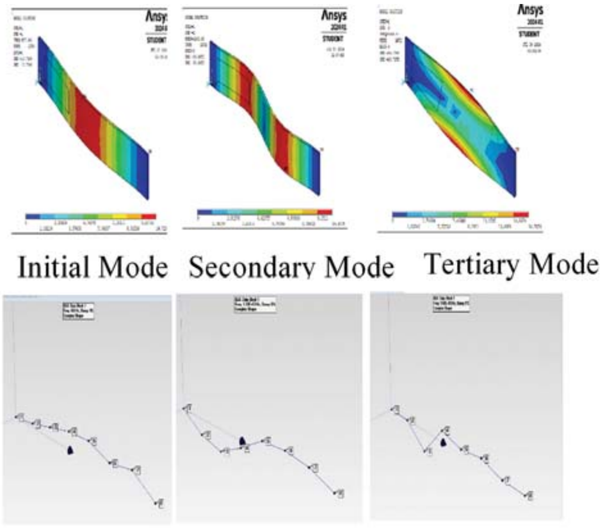

Fig. 10. First three modes of Al beam (C-C) with patch and 12V supply.

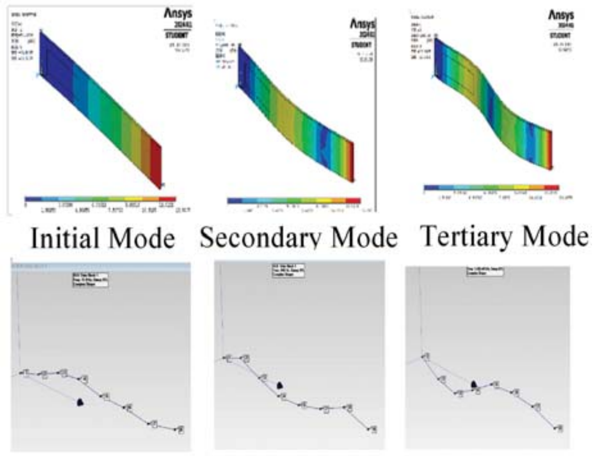

Fig. 11. First three modes of Al beam (S-C) with patch and 12V supply.

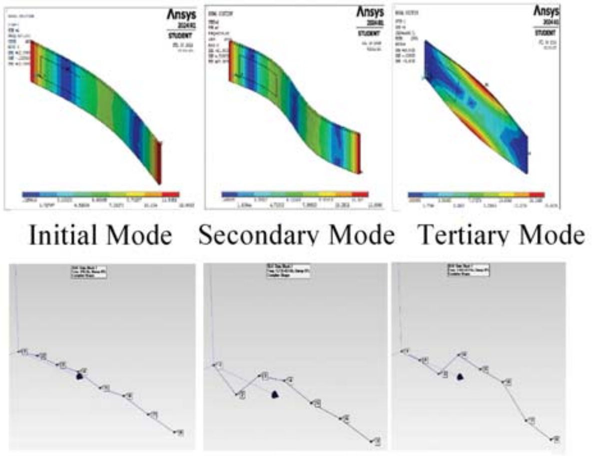

Fig. 12. First three modes of Al beam (S-S) with patch and 12V supply.

5. CONCLUSIONS

The Natural frequencies were studied for the cantilever beam for three different configurations namely, an Aluminium beam, an Aluminium beam with four PVDF patches and an Aluminium beam with four PVDF patches with 12V supply. It is observed that natural frequencies are increasing with mode number.

Our research effectively demonstrates the efficacy of both the numerical and experimental approaches in studying and controlling vibration response in structural members. The close agreement between the numerical simulations and experimental results validates the methods and tools used in our study and providing confidence in their application for active vibration control in various engineering fields. This can be quite useful for the structural health monitoring of the materials to extract the long life of the engineering components.

6. ACKNOWLEDGEMENTS

The authors express their gratitude to the authorities of University College of Engineering Kakinada (A), JNTUK Kakinada for permitting us to use resources (software and hardware) to carry out this research work.

REFERENCES

[1] Yashavantha Kumar, G.Aa. and K.M. Sathish Kumar, 2017. Free vibration analysis of smart composite beam. Materials Today: Proceedings **4.** doi.org/10.1016/j.matpr.2017.02.101

[2] Sharvari, S. Heganna and Jayesh, Joglekar, 2016. Active Vibration Control of Smart Structure using PZT Patches. *Twelfth International Multi-Conference on Information Processing Published by Elsevier (IMCIP-2016).* doi .10.1016/j.procs.2016.06.040.

[3] Kamalpreet, Singh, Saurav, Sharma, Rajeev, Kumar and Mohammad, Talha, 2021. Vibration control of cantilever beam using poling tuned piezoelectric actuator. *Mechanics-Based Design of Structures and Machines,* pp. 1-24. Doi.10.1080/15397734.2021.1891934.

[4] H.I., Schlaberg and J.S. Duffy, Sens, 1994. Actuators A, "Piezoelectric polymer composite arrays for ultrasonic medical imaging applications" *Sensors and Actuators A: Physical,* **44**(2), 111-117.

[5] Li, J., Narita, 2013. Vibration suppression for laminated cylindrical panels with arbitrary edge conditions. *J. Vib. Control,* **19,** 626-640.

[6] K. Bendine, F.B. Boukhoulda, B. Haddag and M. Nouar, 2019. Active vibration control of composite plate with optimal placement of piezoelectric patches. *Gothenburg University Library,* doi.org/10.1080/15376494.2017.1387324.

[7] V. Balamurugan and S. Narayanan, 2001. Shell finite element for smart piezoelectric composite plate/shell structures and its application to the study of active vibration control. *Finite Elements in Analysis and Design,* **37,** doi.org/10.1016/S0168-874X(00)00070-6.

[8] H.S., Tzou and C.I. Tseng, 1991. Distributed modal identification and vibration control of continua: Piezoelectric finite element formulation and analysis. *ASME J. Dyn. Systems, Measurement Control,* p. 113, doi.org/10.1115/1.2896438

[9] Kamalpreet Singh and Saurav Sharma, *et al.,* 2023. Vibration control of cantilever beam using poling tuned piezoelectric actuator. *An International Journal,* **51**(4). https://doi.org/10.1080/15397734.2021.1891934.

The Journal of Acoustical Society of India : Vol. 52, No. 1, 2025 (pp. 25-32)

Development of an empirical model to predict deep groove ball bearing noise

Mrudul P. Wagh, Hariharasudhan M.P., K. Sri Rama Murthy and B. Venkatesham*
Dept. of Mechanical and Aerospace Engineering, IIT Hyderabad, India
e-mail: venkatesham@mae.iith.ac.in

[Received: 07-08-2025; Accepted: 22-08-2025]

ABSTRACT

With advancements in mobility technology, particularly the evolution from Internal Combustion (IC) engines to Electric Vehicles (EV), and the stringent noise and vibration regulations, the automobile industry is increasingly required to consider noise requirements as a design parameter when designing components and subsystems. Several automotive components, such as bearings, wiper motors, power window motors, tires, and side mirrors, need to meet specific noise requirements. This paper focuses on one such component: deep groove ball bearings used in EVs. The study aims to develop simplified empirical relations to correlate the sound pressure level and vibration response of a bearing and predict the sound pressure level (dB) in terms of speed (rpm), load (N), and acceleration level (m/s^2). An experimental bearing test setup has been developed with the capability to vary both speed and load. Appropriate instrumentation has been deployed to measure the vibration and noise radiation from the bearing. The measured experimental data is used to develop an empirical equation. The empirical relation is established based on regression models developed under various loads and speeds, which are the parameters for the system. The multiple regression models are formed using the least squares method. These equations are solved by minimizing errors, leading to matrix formation based on the number of parameters considered, and thus obtaining the unknown coefficients for correlation. The empirical relation developed from the regression equations enables us to predict the sound pressure level (dB) in terms of speed (rpm), load (N), and acceleration level (m/s^2). The proposed empirical model demonstrates a high predictive capability for bearing noise. It will be useful for bearing noise assessment at the design stage.

1. INTRODUCTION

The automotive industry is undergoing a significant transformation with the shift from internal combustion (IC) engines to electric vehicles (EVs). This transition has brought new challenges and opportunities for innovation, particularly in the domain of vehicle acoustics. Traditionally, the noise generated by IC engines masked the sounds emanating from other vehicle components. However, the quieter nature of electric motors has heightened the prominence of noises from ancillary parts, with bearings being one of the notable contributors.

Bearings play a crucial role in various automotive systems by supporting rotating parts and reducing friction. However, they are also sources of noise and vibration, which can detract from the overall driving

---

experience. As the demand for quieter and more efficient EVs grows, addressing these acoustic challenges becomes paramount. The objective of this paper is to establish a correlation between their vibration and noise signatures. By analyzing these signatures across different bearing types, to identify key factors contributing to noise generation and develop strategies for noise mitigation.

Naresh Tandon reviews various vibration and acoustic measurement methods for detecting defects in rolling element bearings. It covers both localized and distributed defect categories, emphasizing vibration measurements in time and frequency domains. Parameters such as RMS level, crest factor, and kurtosis are used effectively, with kurtosis highlighted as particularly useful[1].

Acoustic techniques including sound pressure, sound intensity, and acoustic emission are also discussed, with sound intensity proving superior for bearing diagnostics. Automated data interpretation methods using pattern recognition and neural networks are emerging for efficient defect detection in bearings based on vibration data[1].

Steve J Lacey discussed the multifaceted origins of vibration in rolling bearings, attributing it to factors like manufacturing imperfections, surface defects, and errors in associated components. Vibration and noise are increasingly pivotal in equipment quality assessment and predictive maintenance strategies[2].

Guangwei Yu developed a 4-degree-of-freedom model to study the dynamic behaviour of a 6201 deep groove ball bearing. This model accurately predicts vibration characteristics such as displacement, velocity, and acceleration, with theoretical and simulated frequencies aligning closely with experimental measurements. The study underscores the critical role of structural parameters specifically radial clearance, groove curvature coefficient, and ball diameter on bearing vibration. Increasing radial clearance results in a nonlinear rise in vibration levels, while higher groove curvature coefficients generally amplify vibrations. Additionally, larger ball diameters enhance contact stiffness (K), correlating with increased vibration tendencies[3].

Yuting Hu studied the correlation between noise and vibration during dry milling of aluminium alloy using synchronised acquisition systems. Multiple regression models were established using MATLAB and the least squares method to analyze the effects of milling parameters (spindle speed, milling depth, feed speed) and milling vibration on milling noise[4].

2. METHODOLOGY

The objective of the study was to find the correlation between noise and vibrations. The first direct approach was to try and correlate the noise and vibration signals assuming a linear relationship. But through experimental data and analysis, it can be concluded that no linear correlation exists between them.

Next, a nonlinear correlation between noise and vibration signals which depends upon the varying parameters of the system which are mainly load and rotational speed in this case. For the experiment, the deep groove ball bearing model 6309 is used. The bearing test setup used in the current study is the same as Ajiket[5]. The data is collected for four bearings from three different manufacturers. It consists of three grease bearings and an oil-bearing. For each bearing, the data is collected for three different loads mainly at 200N, 500N, and 1000N, and at six various RPMs varying from 1000 rpm to 6000 rpm with an interval of 1000 rpm. For each test case, two trials are taken to ensure data consistency under the same environmental conditions along with the same operator. The uniaxial accelerometers are mounted on the bearing blocks which are mainly the support bearing blocks and test bearing blocks which acquire the vibration data as shown in Fig. 1. The 1/2" prepolarized free-field condenser microphone is kept at a distance of 0.5m at an angle of 45 degrees from the setup to acquire the sound data. The load cell is mounted between the actuator shaft and stud bolt to monitor and control the load.

The measured vibration acceleration is expressed as rms value and overall sound pressure level for each test case. Figs. 2 to 5 show the measured vibration and acoustic data for all test cases for three manufacturers.

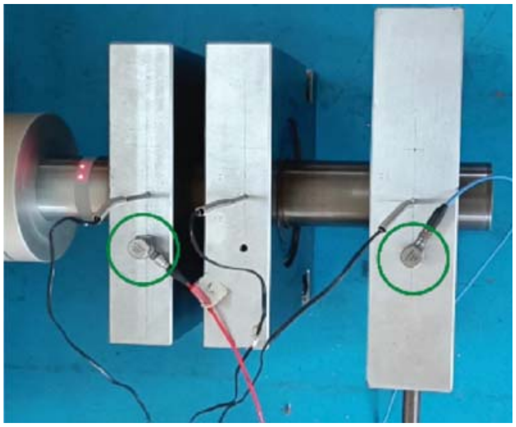

Fig. 1. Experimental accelerometer mounting.

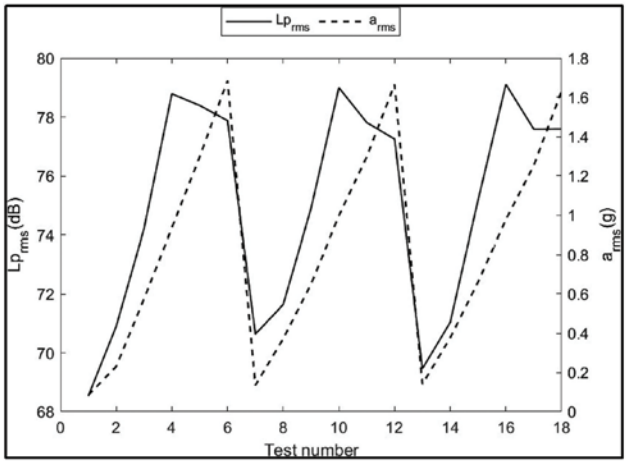

Fig. 2. Measured acoustic and vibration data of manufacturer 1 (MM1) Grease bearing.

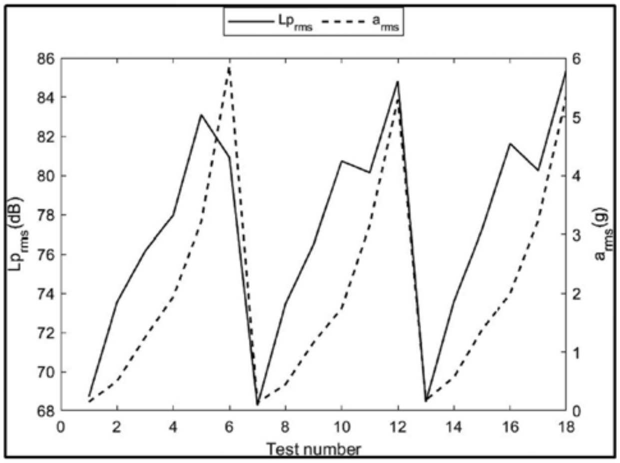

Fig. 3. Measured acoustic and vibration data of manufacturer 2 (MM2) Grease bearing.

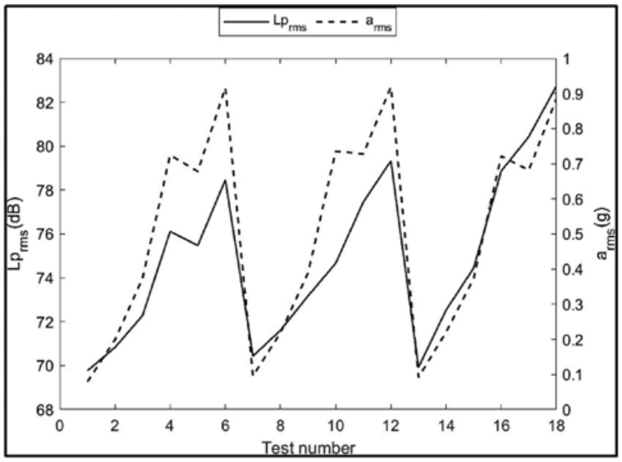

Fig. 4. Measured acoustic and vibration data of manufacturer 3 (MM3) Grease bearing.

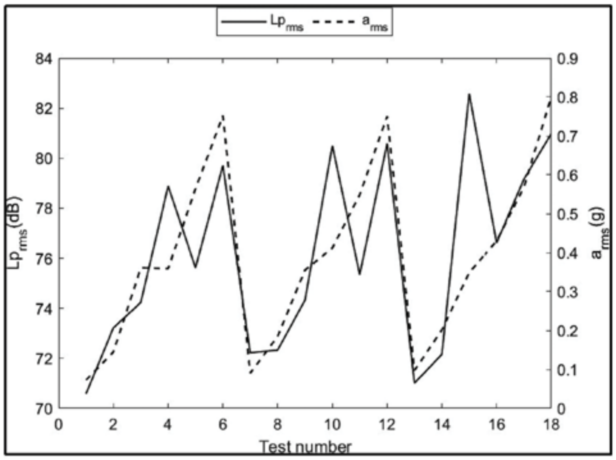

Fig. 5. Measured acoustic and vibration data of manufacturer 3 (MM3) Oil bearing.

From the above plots, it can be observed that there is a strong correlation between noise and vibration signals and the overall variation characteristics curve of SPL and vibration acceleration change with variation of bearing test rig parameters (speed, load), and the trend between SPL and vibration data is almost similar. Based on the above analysis it can be inferred that the test parameters have a significant influence on the bearing sound pressure level (SPL) and overall vibration. The trend of the bearing sound pressure level and vibration acceleration are close to each other.

To further study this correlation between SPL and vibration levels, regression models of test rig SPL between bearing test rig parameters and vibration were established based on the least square method. Fig. 6 shows the flowchart of the proposed correlation study.

Through different combinations of test rig parameters, three regression models were established to study the effects of various parameters on the sound pressure level (SPL) of the test rig.

$$L_p = Cl^x s^y a_{rms}{}^w \tag{1}$$

where,

is the Predicted sound pressure level (dB), C, x, y, w are Coefficients, l is Load(N), s is speed (m/s), and is a_{rms} value of vibration(g).

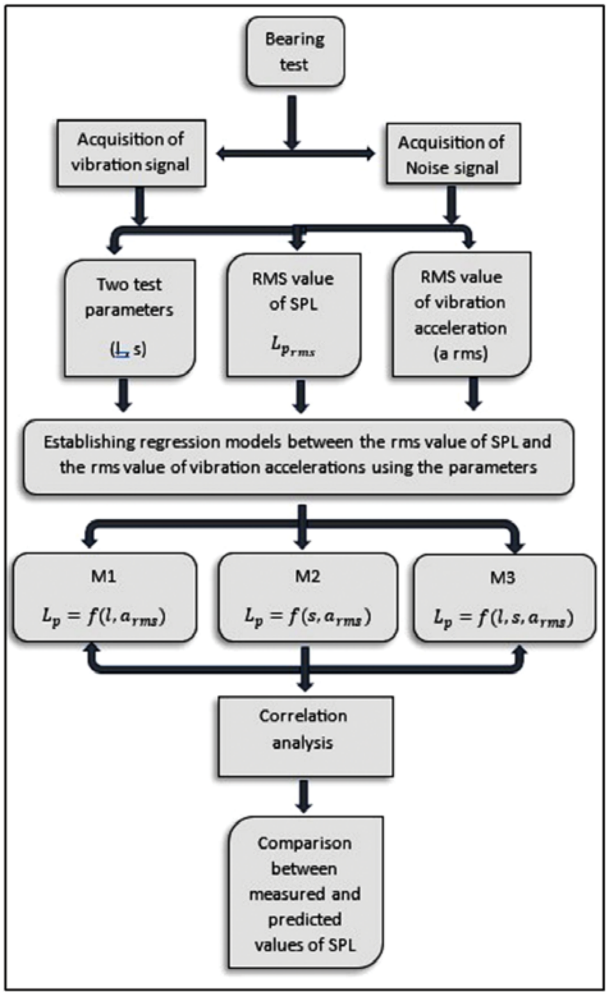

Fig. 6. Flowchart of the correlation study.

The above equation relates the Sound Pressure level (L_p) with the vibration acceleration a_{rms} using the varying parameters - load and speed. This is one of the regression models developed for correlation. The regression models formed along with the parameters involved are mentioned in Table 1.

Based on the above three regression models, the effects of the parameters on the correlation between sound pressure level (SPL) and vibration were studied. Considering the M3 model, based on the least square method, the logarithmic error between measured and predicted value can be written as

$$Error = in\ L_p - in\ L_{prms} = in\ C + x\ in\ l + y\ ins + w\ in\ a_{rms} - in\ L_{prn} \tag{2}$$

Table 1. Regression models.

Model	Total test numbers	Impact Factor			Empirical formula for regression model
		l	s	a_{rms}	
M1	3	✓		✓	$L_p = Cl^x {a_{rms}}^w$
M2	4		✓	✓	$L_p = Cs^y {a_{rms}}^w$
M3	18	✓	✓	✓	$L_p = Cl^x s^y {a_{rms}}^w$

Assuming the sum of logarithmic errors as E based on the least square method the above equation can be written as

$$E = \left\{ x\sum_{i=1}^{n} \ln l_i + y\sum_{i=1}^{n} \ln s_i + w\sum_{i=1}^{n} \ln a_{rms_i} + \ln C - \sum_{i=1}^{n} \ln L_{prms_i} \right\}^2 \tag{3}$$

Further to minimise the errors partially differentiate the above equation with respect to coefficients and equate them to zero. The conditions are mentioned below:

$$\frac{\partial E}{\partial x} = 0;\ \frac{\partial E}{\partial y} = 0;\ \frac{\partial E}{\partial w} = 0;\ \frac{\partial E}{\partial \eta} = 0 \tag{4}$$

After differentiation, Eq. (3) written in matrix form as follows

$$[A]\ [B] = [D] \tag{5}$$

Where,

$$A = \begin{bmatrix} \sum_{i=1}^{n} (\ln l_i)^2 & \sum_{i=1}^{n} \ln s_i \ln l_i & \sum_{i=1}^{n} \ln a_{rms_i} \ln l_i & \sum_{i=1}^{n} \ln l_i \\ \sum_{i=1}^{n} \ln l_i \ln s_i & \sum_{i=1}^{n} (\ln s_i)^2 & \sum_{i=1}^{n} \ln a_{rms_i} \ln s_i & \sum_{i=1}^{n} \ln s_i \\ \sum_{i=1}^{n} \ln a_{rms_i} \ln l_i & \sum_{i=1}^{n} \ln a_{rms_i} \ln s_i & \sum_{i=1}^{n} (\ln a_{rms_i})^2 & \sum_{i=1}^{n} \ln a_{rr} \\ \sum_{i=1}^{n} \ln l_i & \sum_{i=1}^{n} \ln s_i & \sum_{i=1}^{n} \ln a_{rms_i} & \sum_{i=1}^{n} 1 \end{bmatrix} \tag{6a}$$

$$B = \begin{bmatrix} x \\ y \\ w \\ \eta \end{bmatrix} \tag{6b}$$

$$D = \begin{bmatrix} \sum_{i=1}^{n} \ln L_{P_{rms_i}}\ \ln l_i \\ \sum_{i=1}^{n} \ln L_{P_{rms_i}}\ \ln s_i \\ \sum_{i=1}^{n} \ln L_{P_{rms_i}}\ \ln a_{rms_i} \\ \sum_{i=1}^{n} \ln L_{P_{rms_i}} \end{bmatrix};\ \eta = \ln C \tag{6cd}$$

The experimental data are substituted in the matrices *A* and *D*. The values of the regression coefficients *x*, *y*, *w*, and *C* can be obtained by solving for matrix *B*. Furthermore, the correlation coefficient R can be calculated from the regression model obtained and the experimental data.

Similarly, the matrix for the other two regression models can be written as follows-

For regression model M2: The values of *A*, *B*, and *D* are written as follows

$$A = \begin{bmatrix} \sum_{i=1}^{n} (\ln s_i)^2 & \sum_{i=1}^{n} \ln s_i \ln a_{rms_i} & \sum_{i=1}^{n} \ln s_i \\ \sum_{i=1}^{n} \ln s_i \ln a_{rms_i} & \sum_{i=1}^{n} (\ln a_{rms_i})^2 & \sum_{i=1}^{n} \ln a_{rms_i} \\ \sum_{i=1}^{n} \ln s_i & \sum_{i=1}^{n} \ln a_{rms_i} & \sum_{i=1}^{n} 1 \end{bmatrix} \tag{7a}$$

$$B = \begin{bmatrix} y \\ w \\ \eta \end{bmatrix} \tag{7b}$$

$$D = \begin{bmatrix} \sum_{i=1}^{n} \ln L_{P_{rms_i}} \ln s_i \\ \sum_{i=1}^{n} \ln L_{P_{rms_i}} \ln a_{rms_i} \\ \sum_{i=1}^{n} \ln L_{P_{rms_i}} \end{bmatrix}; \eta = \ln C \tag{7cd}$$

For regression model M1: The values of A, B, and D are written as follows

$$A = \begin{bmatrix} \sum_{i=1}^{n} (\ln l_i)^2 & \sum_{i=1}^{n} \ln l_i \ln a_{rms_i} & \sum_{i=1}^{n} \ln l_i \\ \sum_{i=1}^{n} \ln l_i \ln a_{rms_i} & \sum_{i=1}^{n} (\ln a_{rms_i})^2 & \sum_{i=1}^{n} \ln a_{rms_i} \\ \sum_{i=1}^{n} \ln s_i & \sum_{i=1}^{n} \ln a_{rms_i} & \sum_{i=1}^{n} 1 \end{bmatrix} \tag{8a}$$

$$B = \begin{bmatrix} x \\ w \\ \eta \end{bmatrix} \tag{8b}$$

$$D = \begin{bmatrix} \sum_{i=1}^{n} \ln L_{P_{rms_i}} \ln s_i \\ \sum_{i=1}^{n} \ln L_{P_{rms_i}} \ln a_{rms_i} \\ \sum_{i=1}^{n} \ln L_{P_{rms_i}} \end{bmatrix}; \eta = \ln C \tag{8cd}$$

The B matrix in Eq. (5) is solved for three different regression models and the regression coefficients matrix was calculated for all the respective models.

3. RESULTS AND DISCUSSION

The above matrices are solved for different regression models (M1, M2, M3) to get the coefficient matrix B which consists of values for the regression coefficients to predict the noise from the system parameters. The final regression model results are compiled in the Table 2 below.

It can be observed from Table 2 that R^2 is the coefficient of correlation which is obtained by comparing the experimental values of Sound pressure levels (SPL) with the SPL obtained from regression models for the respective cases. The major focus of this correlation lies in the M3 regression model as it involves the effect of varying parameters on the predicted noise (SPL) and Vibration levels. The plots between predicted and experimental SPL values for the M3 model are shown in Figs. 7 to 10. There is a good correlation between the predicted and experimental measured data.

Table 1. Final results for regression models.

Bearing type	Regression model	Empirical formula for regression model	Bearing make	R^2
Grease	M1	$L_p = 63.49 l^{0.0272} a_{rms}^{0.0775}$	MM1	0.9
			MM2	0.91
			MM3	0.88
	M2	$L_p = 57.1867 s^{0.1517} a_{rms}^{-0.0302}$	MM1	0.91
			MM2	0.98
			MM3	0.94
	M3	$L_p = 65.7437 l^{0.00774} s^{0.065} a_{rms}^{0.0351}$	MM1	0.9
			MM2	0.97
			MM3	0.9
Oil	M1	$L_p = 79.4199 l^{0.0184} a_{rms}^{0.1559}$	MM3	0.99
	M2	$L_p = 59.398 s^{0.1009} a_{rms}^{0.0086}$	MM3	0.92
	M3	$L_p = 52.198 l^{0.02616} s^{0.1039} a_{rms}^{0.0246}$	MM3	0.94

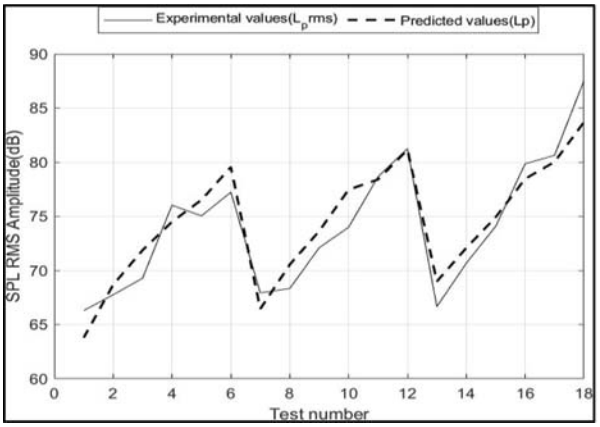

Fig. 7. For oil-bearing, R^2 = 0.94, Model - M3.

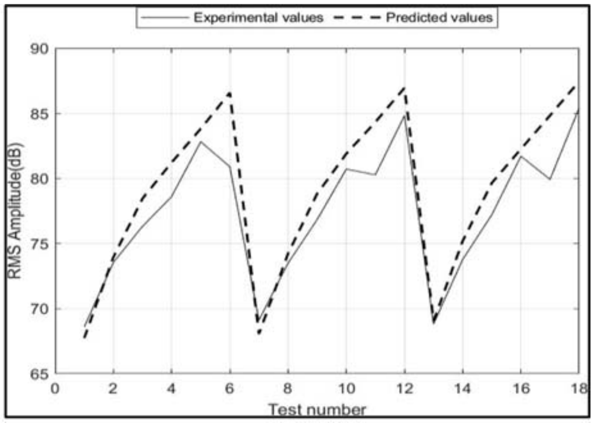

Fig. 8. For Grease bearing MM1, R^2 = 0.97, Model - M3.

4. SUMMARY

An empirical model was developed to predict the sound pressure level (SPL) based on experimental data involving speed, load, and vibration. The correlation coefficient (R^2) consistently exceeded 0.9, indicating a strong relationship between bearing SPL, speed, load, and vibration. The predicted values closely matched the experimental data. The study also considered the impact of speed and load on both SPL and vibration. To overcome the limitations of the proposed model, future work should include additional test cases that incorporate different types of bearings, as well as a wider range of load and speed conditions.

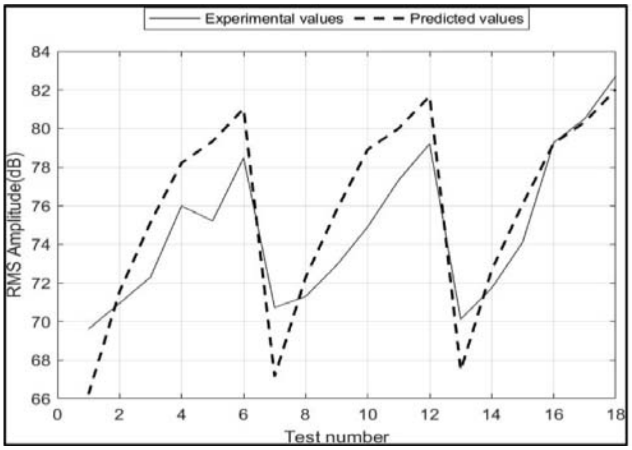

Fig. 9. Grease bearing MM2, $R^2 = 0.9$, Model - M3.

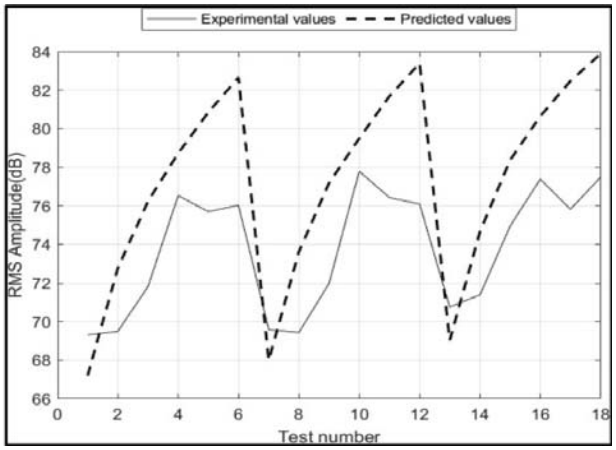

Fig. 10. Grease bearing MM3, $R^2 = 0.9$, Model -M3.

5. ACKNOWLEDGEMENT

The authors would like to thank Indian Institute of Technology Hyderabad and Ministry of Heavy Industry for providing the financial support and resources to conduct the current research work.

REFERENCES

[1]. Naresh Tandon and Achintya Choudhury, 1999. A review of vibration and acoustic measurement methods for the detection of defects in rolling element bearings, *Tribology international*, **32**(8), 469-480.

[2]. Steve J. Lacey, 2008. An overview of bearing vibration analysis, *Maintenance & asset management*, **23**(6), 32-42.

[3]. Yuting Hu, Shuncai Li, Xing Deng and Slatin Vadim, 2022. Correlation analysis of noise sound pressure and vibration in aluminium alloy milling, *Journal of Vibration and Control*, **28**(3-4), 276-289.

[4]. Guangwei Yu, Rui Wu and Wei Xia, 2018. Influence of structural parameters of deep groove ball bearings on vibration, *In AIP Conference Proceedings*, **1955**. AIP Publishing.

[5]. Ajiket and B. Venkatesham, 2023. Vibration and acoustic signal monitoring of high-speed bearings for electrical vehicle, *NCCM-2023*, Vizag.

The Journal of Acoustical Society of India : Vol. 52, No. 1, 2025 (pp. 33-41)

Nonlinear sound-structure inter action in a 2D flexible wave guide with uniform mean flow

Manish Dwivedi and Venkata R. Sonti

Department of Mechanical Engineering, IISc Bengaluru-560 012, India

e-mail: manishd@iisc.ac.in

[Received: 04-08-2025; Accepted: 22-08-2025]

ABSTRACT

In this semi-analytical investigation, nonlinear wave propagation in an infinite 2D wave guide is considered. This waveguide has a flexible plate as one of the boundaries, while the other boundary is rigid. The wave guide carries an acoustic fluid with mean flow. Nonlinear acoustic and structural equations are used to describe the system. The regular perturbation method is used to separate the equations at the first and second orders. At the first order, the dispersion equation is obtained, which results in the primary waves. It is found that the magnitude of the primary wave numbers in the wave guide decreases as the Mach number increases. The closed-form solution for pressure and in-plane plate displacement at nonlinear order is obtained. Self and cross-mode interactions of the waves are discussed. In self-mode interactions, the primary waves with the same mode number interact with each other, while in cross-mode cases, the waves with different mode numbers interact. The conditions for resonance and beats for the in-plane plate displacements and second-order pressure solutions are obtained. The effect of the Mach number on resonance and beats is also investigated.

1. INTRODUCTION

Nonlinear wave propagation in wave guides is observed in applications such as exhaust pipes, jet engines, oceanic wave guides, and blood flow in veins. In these wave guides, harmonic excitation causes multiple harmonic waves and modes to propagate at the excitation frequency determined by the dispersion relation. These modes, whether planar or non-planar, interact due to weak nonlinearity, generating higher harmonics that either grow spatially or alternate in growth and decay. Most studies focus on rigid wave guides, while some consider flexibility but assume no mean flow of the fluid[1,2,4-7,11]. Even in cases where mean flow is considered, the analysis remains limited to rigid waveguides[8-10]. Research on nonlinear wave propagation in flexible wave guides with mean flow is limited and requires further investigation.

In this paper, nonlinear wave propagation in an acoustic wave guide is investigated. The self-mode and cross-mode interactions of waves are studied, and the conditions for beats and resonance are determined.

2. PROBLEM FORMULATION

A 2D semi-infinite wave guide carrying uniform mean flow is considered. The top boundary ($x^* = a^* + w^*$) is a flexible plate, and the lower boundary ($x^* = 0$) is rigid. There is a piston source of height d^*, oscillating harmonically at frequency ω, located at the origin ($z^* = 0$), which excites sound in higher modes (see Fig. 1). The flow field velocity is decomposed into a steady mean part and an acoustic part as $\vec{V}^*(x, z, t) = U^*\hat{k} + \vec{v}^* * (x, z, t)$. Consequently, the total velocity potential is also decomposed as $\phi^*(x, z, t) = \phi^*(x, z, t) + U^*z$. Here, $\vec{v}^*$ and ϕ^* are the acoustic variables. The fluid is assumed to be in viscid, and hence, the flow is irrotational ($\vec{v}^* = \nabla^*\phi^*$). The analysis is conducted for subsonic flow ($M < 1$), and only forward propagating modes are considered.

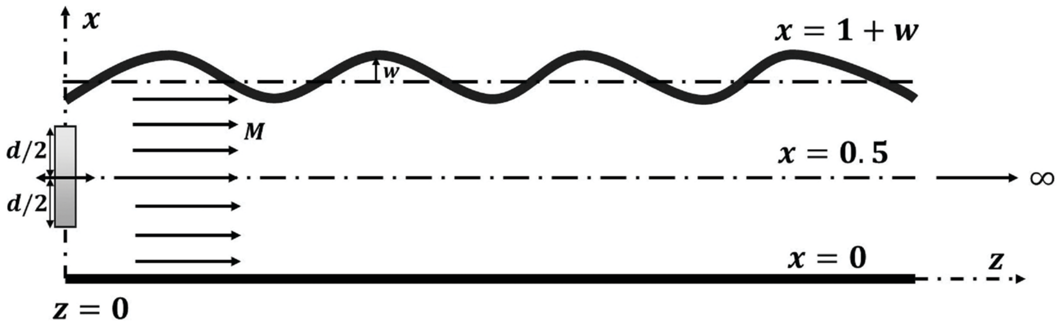

Fig. 1. 2D wave guide bounded by a flexible plate on one side and a rigid wall on the other side and carrying the mean flow.

The following set of non-dimensional variables is used, where the superscript (*) denotes the dimensional quantity:

$$x - \frac{x^*}{a^*}, z - \frac{z^*}{a^*}, w - \frac{w^*}{a^*}, u - \frac{u^*}{a^*}, d - \frac{d^*}{a^*}, t - \frac{t^* c_0}{a^*}$$

$$p = \frac{p^*}{\rho_0 c_0}, \emptyset = \frac{\emptyset^*}{c_0 a^*}, M = \frac{U^*}{c_0}, \Omega = \frac{\omega a^*}{c_0}, \nabla = a^* \nabla^*$$

Here, a^* is the height of the wave guide, ϕ is the non-dimensional acoustic velocity potential, c_0 is the sound speed at infinitesimal amplitude, and w and u are the non dimensional transverse and in-plane plate displacements, respectively. All equations from here on are written in terms of non-dimensional quantities.

The nonlinear convective acoustic wave equations for the in viscid polytropic gas are given by:[9,10]

$$\mu V^2 \emptyset - M^2 \frac{\partial^2 \emptyset}{\partial z^2} - 2M \frac{\partial^2 \emptyset}{\partial z \partial t} - \frac{\partial^2 \emptyset}{\partial t^2} = N_1(\emptyset) \tag{1}$$

$$N_1(\emptyset) - (\gamma - 1)(\emptyset_t + M\emptyset_z)\nabla^2\emptyset + 2\nabla\emptyset.(\nabla\emptyset_t + M\nabla\emptyset_z)$$

Here, $\mu = 1 - \frac{(\gamma - 1)}{2} M^2$ is a factor accounting for compressibility. In the conventional convective wave equation $\mu = 1$ is used[1,8,9]. M is the Mach number of the flow.

The velocity potential and acoustic pressure are related as follows:

$$p = -\frac{\partial \emptyset}{\partial t} - M\frac{\partial \emptyset}{\partial z} + \frac{|\nabla \emptyset|^2}{2} - \left(\frac{\partial \emptyset}{\partial t} + M\frac{\partial \emptyset}{\partial z}\right)^2 \tag{2}$$

Nonlinear plate equations for in-plane and transverse motions at $x = 1 + w$ are given by:[5,6]

$$\frac{\partial^2 u}{\partial z^2} + \frac{\partial w}{\partial z}\,\frac{\partial^2 w}{\partial z^2} - \frac{1}{c^2}\,\frac{\partial^2 u}{\partial t^2} = 0 \tag{3a}$$

$$c^2\eta^2\frac{\partial^4 w}{\partial z^4}+\frac{\partial^2 w}{\partial t^2} = vp\big|_{x=1+w} + \frac{\partial^2 u}{\partial t^2}\,\frac{\partial w}{\partial z} + c^2\left[\frac{\partial u}{\partial z}\frac{\partial^2 w}{\partial z^2} + \frac{1}{2}\left(\frac{\partial w}{\partial z}\right)^2\frac{\partial^2 w}{\partial z^2}\right] \tag{3b}$$

Here, $\eta^2 = \frac{t_S^2}{12a^{*2}}$, $c = \frac{c_S}{c_0}$, $C_S = \left(\frac{E_S}{\rho_S(1-v_0^2)}\right)^{\frac{1}{2}}$ and $v = \frac{\rho_o^* a^*}{\rho_S^* t_S^*}$ are the thickness parameter, the relative wave speed in the plate, the wave speed in the plate, and the fluid loading parameter, respectively. Here, ρ_s, t_s, E_s and v_0 are the density of the plate, the thickness of the plate, the Young's modulus, and the Poisson's ratio of the plate material, respectively. The fluid loading parameter represents the coupling between the fluid and the structure.

At the fluid-structure interface, the velocity of the structure must be equal to the velocity of the fluid particle in the normal direction. The boundary conditions at the flexible and rigid boundaries are given as follows:[3,5]

$$\left.\frac{\partial \emptyset}{\partial x}\right|_{x=1+w} = \frac{\partial w}{\partial t} + M\frac{\partial w}{\partial z} + \frac{\partial w}{\partial z}\left.\frac{\partial \emptyset}{\partial z}\right|_{x=1+w} \tag{4a}$$

$$\left.\frac{\partial \phi}{\partial x}\right|_{x=0} = 0 \tag{4b}$$

The source condition at $z = 0$ is given by

$$p(x, z=0, t) = \varepsilon\, p_0 g(x)\cos(\Omega t) \tag{5}$$

where, $g(x) = \left[H\left(x-\left(1-\frac{d}{2}\right)\right) - H\left(x-\frac{1+d}{2}\right)\right]$ is the piston profile, p_0 is the pressure amplitude and ε is a book-keeping parameter. A regular perturbation method is used to obtain the equations at linear and nonlinear orders. The $O(\varepsilon^2)$ terms are assumed to be much less than $O(\varepsilon)$ terms. The total solution is expanded as follows:[2,11]

$$\phi(x,z,t) = \sum_{i=1}^{2}\frac{1}{2}\left(\epsilon^2 \emptyset_i(x,z)\exp(ji\Omega t) + cc\right) \tag{6a}$$

$$p(x,z,t) = \sum_{i=1}^{2}\frac{1}{2}\left(\epsilon^2 p_i(x,z)\exp(ji\Omega t) + cc\right) \tag{6b}$$

$w(z, t)$ and $u(z, t)$ are also expanded in similar fashion. Here Ω is the non-dimensional excitation frequency, "*j*" is iota and "*c*" represents the complex conjugate. Substituting Eqs. [(6a)-(6b)] into Eqs. [(1)-(5)], we obtain the equations at linear [$O(\varepsilon)$] and nonlinear [$O(\varepsilon^2)$] orders. At the linear order, the obtained solutions are as follows:

$$\phi_1(x,z) = \sum_{r=0}^{\infty} A_r\cos(\alpha_r.x)e^{-jk_r z} \tag{7a}$$

$$p_1(x,z) = \sum_{r=0}^{\infty} -jA_r\,(\Omega - Mk_r)\cos(\alpha_r.x)e^{-jk_r z} \tag{7b}$$

$$w_1(z) = \sum_{r=0}^{\infty}\frac{IA_r}{\Omega - Mk_r}\,\alpha_r\sin(\alpha_r)e^{-jk_r z} \tag{7c}$$

$$u_1 = A_u e^{-jk_u z} \tag{7d}$$

Here, $k_u = \frac{\Omega}{c}$ is the in-plane plate wave number, while k_r and α_r represent the non-dimensional axial and cross-sectional wave numbers for the r^{th} mode, respectively. These wave numbers are related through the equation $R(k_\mathrm{r}, \alpha_\mathrm{r}, \Omega) = 0$ where, $R(k_\mathrm{r}\ \alpha_\mathrm{r}, \Omega) = (M^2 - \mu)k_\mathrm{r}^2 - 2Mk_\mathrm{r}\Omega - \mu\alpha_\mathrm{r}^2 + \Omega^2)$. Solving this equation for the axial wave number k_r, we obtain:

$$k_u = \frac{-M\Omega \pm \left[\mu(\Omega^2 - (\mu - M^2)\alpha_r^2\right]^{\frac{1}{2}}}{\mu - M^2} \tag{8}$$

If we constrain M to be positive in Eq. (8), the plus sign corresponds to the axial wave number for downstream propagation, while the minus sign represents the wave number for upstream propagation. By setting $\mu = 1$ (for incompressible fluids), we obtain the same equation for the axial wave number as derived by Morfey[1] and Munjal[8]. In our analysis, we have focused exclusively on waves propagating in the downstream direction. The Eqs. [(7a)-(7d)] represent the primary waves in the waveguide in the r^{th} mode, excited at frequency Ω. These primary waves satisfy the Dispersion equation given by:

$$D(k_r,\ \alpha_\mathrm{r}, \Omega) = (c^2\eta^2 k_r^4 - \Omega^2)\ \alpha_\mathrm{r}\ \sin(\alpha_\mathrm{r}) + v\cos(\alpha_\mathrm{r})(\Omega - Mk_\mathrm{r})^2 = 0 \tag{9}$$

Eq. (9) can be solved to obtain the coupled axial (k_r) and cross-sectional (α_r) wave numbers. For $v = 0$, solving Eq. (9) yields the uncoupled wave numbers, where

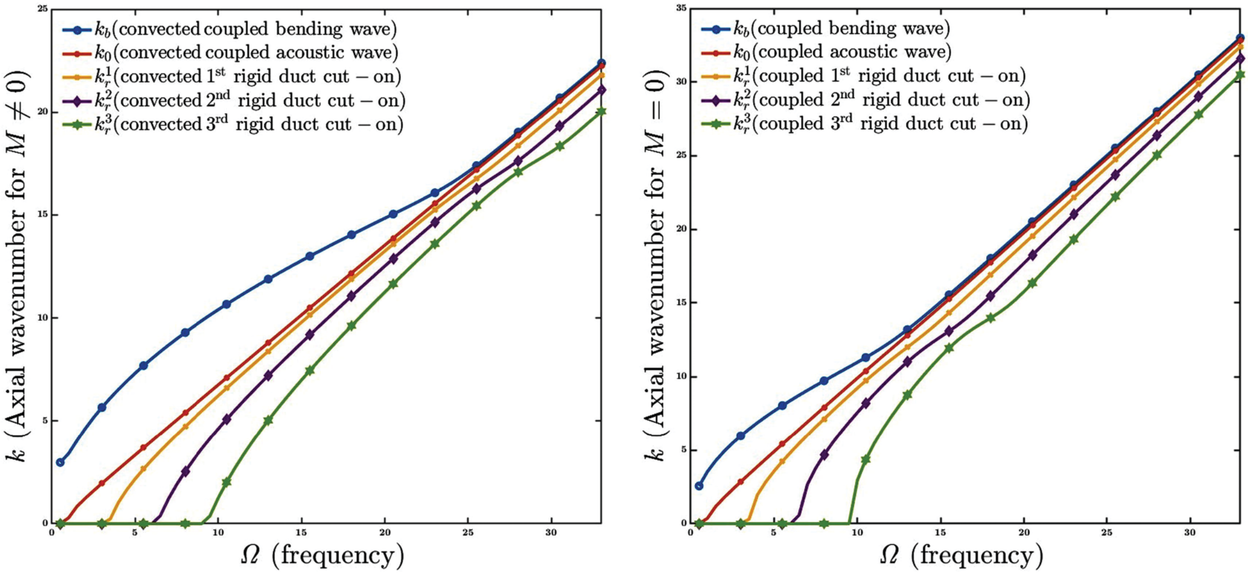

(a) (b)

Fig. 2. The dispersion curve for $\gamma = 1.4$, $c = 6.5$, $\eta = 0.05/\sqrt{12}$, $v = 1.25(a)$ with mean flow (M=0.5), (b) without mean flow M=0.

The first term represents the uncoupled bending wave (k_b^u), the second term represents the acoustic plane wave (k_0^u), and the third term represents the uncoupled n^{th} rigid duct cut-on (k_r^{nu}). The coupled wave numbers $[k_b, k_0, k_r^n (n = 1, 2, 3, ...)]$ are found numerically and plotted in Fig. 2 for cases with and without mean flow. The results for M=0 match the results obtained by Bharat *et al.*[6]. It is found that the axial wave numbers in the wave guide with mean flow (M≠0) are lower than those without mean flow (M=0) due to convective effects. The phase speed of a wave r^{th} is given by $c_p^{(r)} = \Omega/k_\mathrm{r}$ (see Fig. 3). Similarly, the group speed is defined as $c_p^{(r)} = \left(\frac{\partial k_r}{\partial \Omega}\right)^{-1}$. The relationship between the phase speed and group speed is given by $(c_p - M)(c_g - M) = \mu$. The cut-on frequency is the frequency at which the group velocity c_g

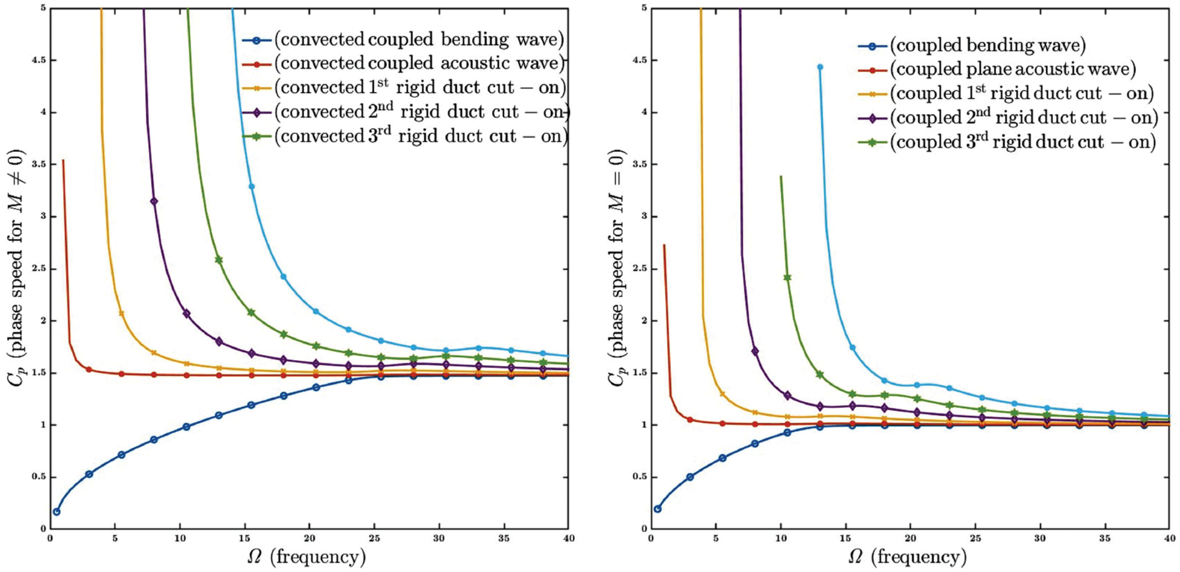

(a) (b)

Fig. 3. The dispersion curve for $\gamma = 1.4$, $c = 6.5$, $\eta = 0.05/\sqrt{12}$, $v = 1.25$*(a)* with mean flow (M=0.5), *(b)* without mean flow M=0.

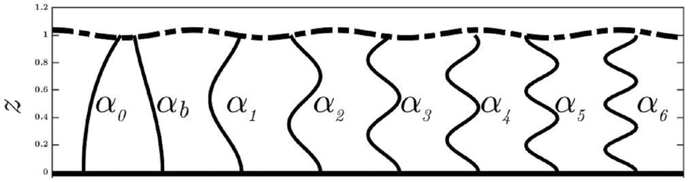

Fig. 4. Cross-sectional modes in the waveguide.

becomes zero. The presence of mean flow lowers the cut-on frequencies of modes compared to the case without mean flow. The dispersion curve also indicates that at a particular excitation frequency, waves in various modes exist in the wave guide (see Fig. 4). The first-order modal amplitudes A_r can be obtained from the source condition. Additionally, since the fluid is inviscid, $A_u = u_1 = 0$, and hence, the in-plane plate waves cannot be excited.

3. SOLUTION AT NONLINEAR ORDER

The solutions at nonlinear order for pressure and in-plane plate displacements are given as follows:

$$\begin{aligned} p_2 = &\sum_{p=0}^{\infty} 2\Omega F_p \cos\left(\alpha_{2,p}.x\right) e^{-jk_{2,p}.z} \\ &+ \sum_{r,s=0}^{\infty} 2\Omega\ A_r A_s \left\{\frac{C_1^{rs}}{E_1^{rs}} + \frac{C_5^{rs}}{2\Omega}\right\} \cos((\alpha_r - \alpha_s)\ x)\ e^{-j(k_r+k_s)z} \\ &+ \sum_{r,s=0}^{\infty} 2\Omega\ A_r A_s \left\{\frac{C_2^{rs}}{E_2^{rs}} + \frac{C_6^{rs}}{2\Omega}\right\} \cos((\alpha_r - \alpha_s)\ x)\ e^{-j(k_r+k_s)z} \\ &+ \sum_{r,s=0}^{\infty} 2\Omega \frac{A_r A_s}{D_3^{rs}} \left[\frac{C_3^{rs}}{4\Omega^2} - \frac{C_1^{rs}}{E_1^{rs}} D_1^{rs} - \frac{C_2^{rs}}{E_2^{rs}} D_2^{rs}\right] \cos\left((\tilde{\alpha}_{rs})x\right) e^{-j(k_r+k_s)z} \end{aligned} \tag{10}$$

$$u_2 = \sum_{r,s=0}^{\infty} A_r \; A_s \frac{C_6^{rs}}{(K_r + k_s)^2 - k_{2,u}^2} \, [e^{-j(k_r + k_s)z} - \mathrm{e}^{-\mathrm{j}k_{2,u}z}] \tag{11}$$

Here,

$$E_1^{rs} = R(k_r + k_s, \alpha_\mathrm{r} - \alpha_\mathrm{s}, 2\Omega) \tag{12}$$

$$E_2^{rs} = R(k_r + k_s, \alpha_\mathrm{r} - \alpha_\mathrm{s}, 2\Omega) \tag{13}$$

$$D_1^{rs} = D(k_r + k_s, \alpha_\mathrm{r} - \alpha_\mathrm{s}, 2\Omega) \tag{14a}$$

$$D_2^{rs} = D(k_r + k_s, \alpha_\mathrm{r} - \alpha_\mathrm{s}, 2\Omega) \tag{14b}$$

$$D_3^{rs} = D(k_r + k_s, \tilde{\alpha}_\mathrm{rs}, 2\Omega) \tag{14c}$$

At O(ε^2), the excitation frequency is 2Ω. Due to the flexibility of the wave guide, a set of cross-sectional wave numbers $\alpha_{2,p}$ and axial wave numbers $k_{2,p}$ are generated. The relation between $\alpha_{2,p}$ and $k_{2,p}$ is given by $R(k_{2,p}, \alpha_{2,\mathrm{p}}, 2\Omega) = 0$. The homogeneously generated wave numbers at 2Ω satisfy the dispersion equation $D(k_{2,p}, \alpha_{2,\mathrm{p}}, 2\Omega) = 0. \tilde{\alpha}_{rs}$ satisfies the relation $R(k_r + k_s, \; \alpha_r - \alpha_s, \; 2\Omega) = 0$. The constants $C_i^{r,s}$ $(for \; i = 1,2,3,.....)$ are functions of Ω, η, v, α_j, k_j $(j = r, s)$ and M (expressions are not provided due to page constraints).

4. RESULTS AND DISCUSSIONS

Looking at Eq. (10), it seems that p_2 will blow up when $E_1^{r,s}$, $E_2^{r,s}$, and $\mathrm{D}_3^{r,s}$ become zero. However, it can be seen from Fig. 5 that $E_1^{r,s}$ never goes to zero, and when $E_2^{r,s} = 0$ (which happens only in the case of self-mode interactions $r = s$), its effect is cancelled out by the solution due to the flexible boundary (square bracketed term in Eq. (10)), and the total solution is stable. Thus, the pressure solution becomes resonant only when $D_3^{r,s} = 0$, and the resonant frequencies can be found in Fig. 6b. At these frequencies, $\delta k = k_r + k_s - k_{2,p} = 0^4$ (though results of pressure resonance are not included in this paper). When $D_3^{r,s} \neq 0$, the pressure solution beats spatially, and the beating length is given by $L_{beat} = \frac{2\pi}{|\delta k|}$. As seen in Fig. 7b, $D_3^{r,s} = 0$

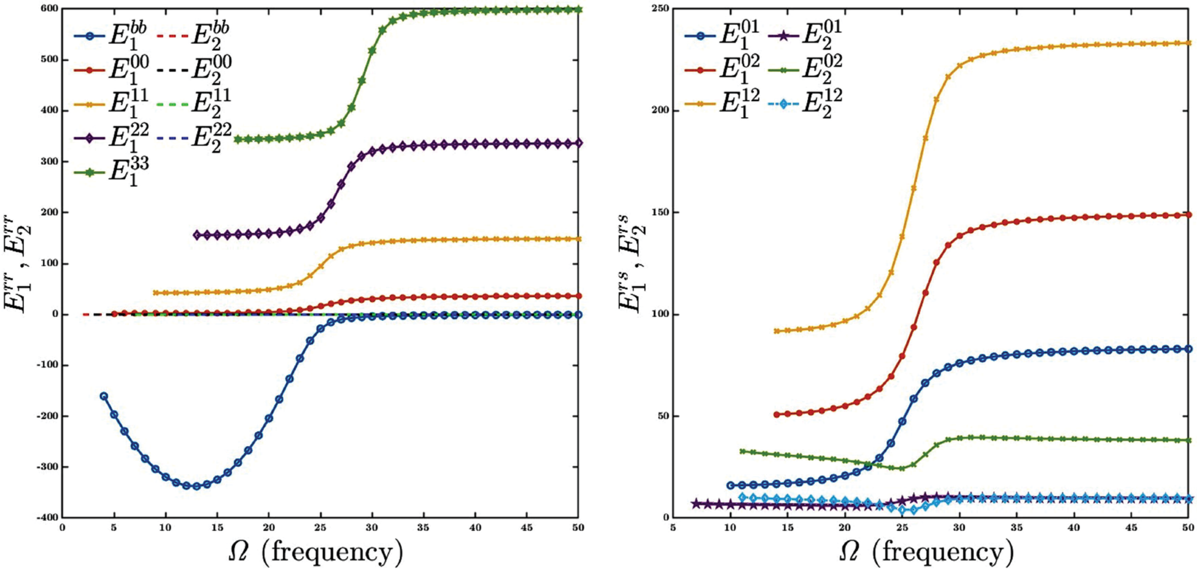

(a) (b)

Fig. 5. $E_1^{r,s}$ and $E_2^{r,s}$ for (a) self-mode ($r = s$) interactions, (b) cross-mode interactions ($r \neq s$).

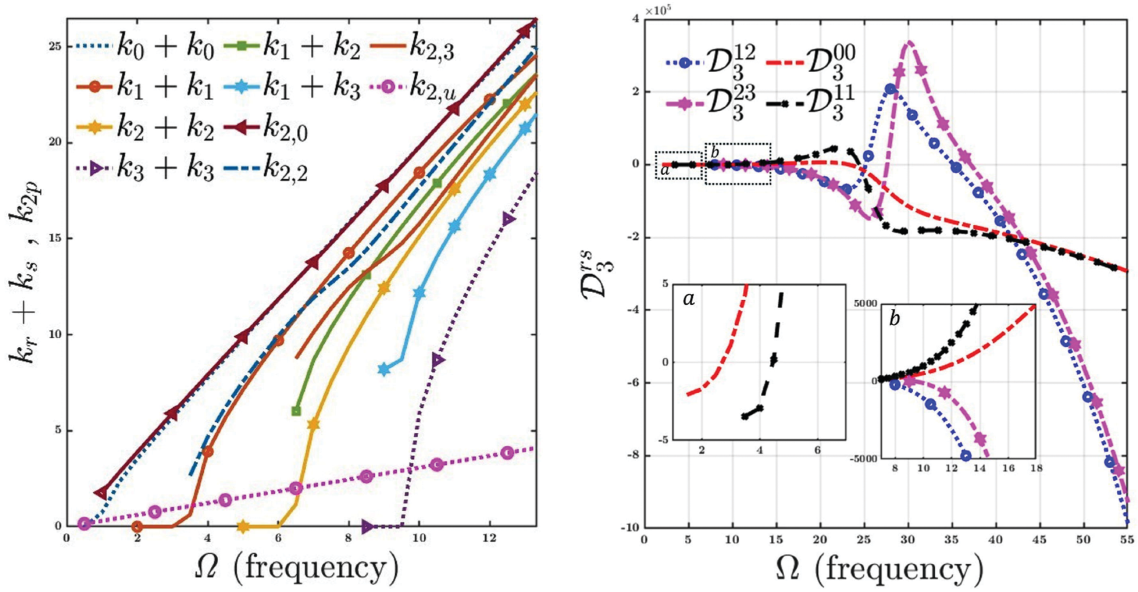

(a) (b)

Fig. 6. (a) Interactions of homogeneous ($k_{2,p}$) and forced ($k_r + k_s$) wave numbers, (b) $D_3^{r,s}$ for self and cross-mode interactions ($r \neq s$).

goes to zero for self-mode (r=s) as well as for cross-mode (r≠s) interactions. Hence, pressure resonant interactions occur for both self- and cross-mode interactions. The amplitude of the pressure solution is inversely proportional to the amplitude of $\left|D_3^{r,s}\right|$.

Similarly, for the in-plane plate displacement u_2, when $\delta k = k_r + k_s - k_{2,p} = 0$, it becomes resonant (see Eq. (11)). When $k_r + k_s - k_{2,p} \neq 0 (\delta k \neq 0)$, it exhibits beating behavior. The result for plate in-plane resonance is shown in Fig. 7a. At Ω = 3.5, the mode for which $r = s = 1$ and $2k_1 = k_{2,u}$ (see Fig. 6a) becomes resonant, while other modes beat with a beating length $L_{beat} = \frac{2\pi}{|\delta k|}$. Additionally, Fig. 6a shows that for crossmode

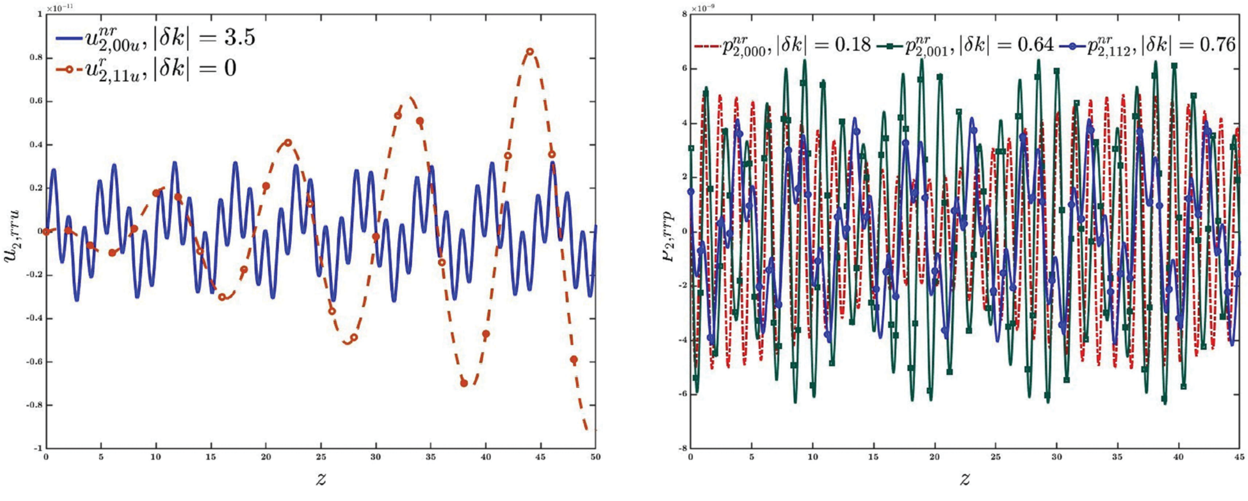

(a) (b)

Fig. 7. (a) The resonant and non-resonant in-plane plate displacement at Ω=3.55, (b) The non-resonant pressure solution at Ω=3.55.

interactions ($r \neq s$), $k_r + k_s \neq k_{2,u}$. Hence, there is no in-plane plate resonance for cross-mode interactions, and only a beating solution exists.

At this frequency, $D_3^{r,s} \neq 0 (\delta k \neq 0)$, and hence the nonlinear pressure solution exhibits beating. The pressure solution for self-mode interactions is shown in Fig. 7b.

5. EFFECT OF MACH NUMBER ON RESONANCE FREQUENCY

In Fig. 8, $D_3^{r,s}$ for various Mach numbers and for self and cross-mode interactions are plotted. $D_3^{r,s}$ crosses zero at certain frequencies, and these resonant frequencies are affected by the mean flow. As M increases, the resonant frequency goes up in value. At higher excitation frequencies, $D_3^{r,s} \neq 0$, and hence the pressure solutions are free of resonances.

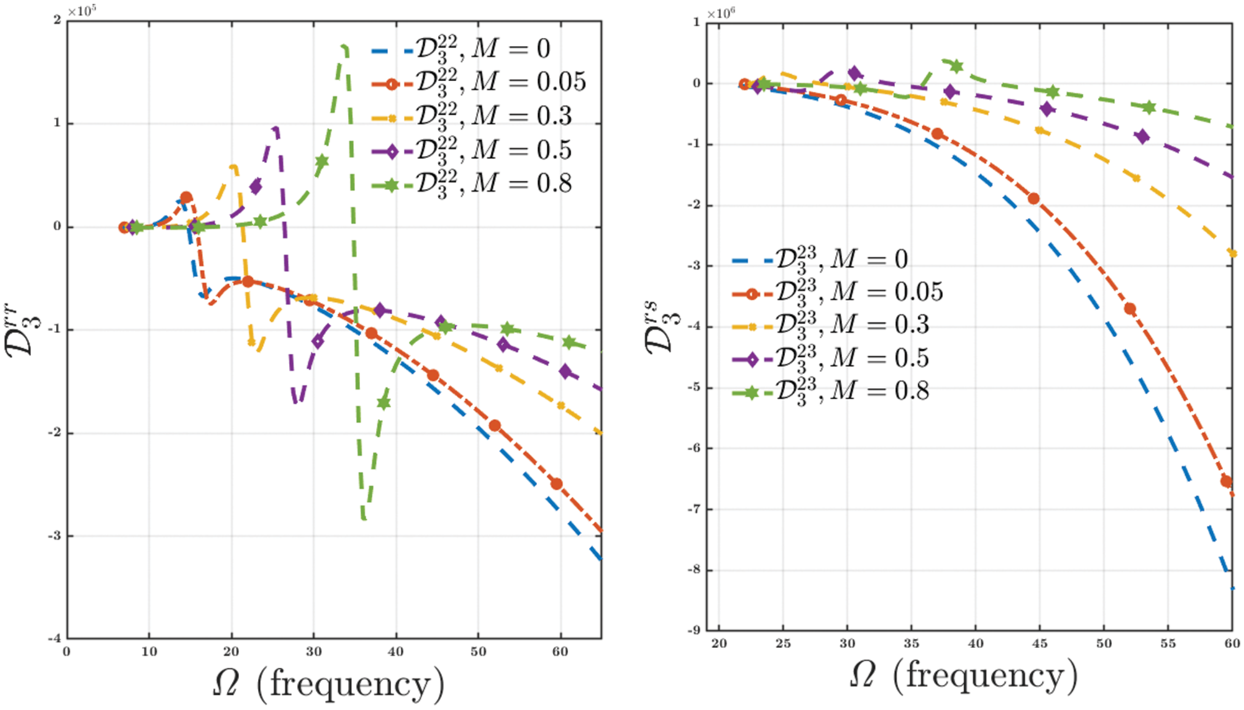

(a) (b)

Fig. 8. $D_3^{r,s}$ and $D_3^{r,s}$ for (a) self-mode $(r = s)(k_{2,p})$ interactions, (b) cross-mode interactions ($r \neq s$).

5. CONCLUSIONS

In this study, nonlinear wave propagation in a 2D infinite flexible waveguide is investigated. It is found that the primary axial wave numbers in the waveguide get reduced in magnitude due to the convective effects of the mean flow compared to the wave numbers without mean flow. In self-mode interactions, resonances occur in pressure and in-plane plate displacement at different frequencies. In cross-mode interactions, pressure resonance occurs, but there is no in-plane plate resonance. Mostly, the waveguide exhibits beats. The beat amplitude and beat length depend upon the difference in forced and homogeneous wave numbers. When the Mach number is increased, the natural frequencies also increase, and at a larger excitation frequency, the number of resonant interactions drastically reduces. The results for M=0 match the results of Bharat *et al.*[6].

REFERENCES

[1]. C. L. Morfey, 1971. Sound transmission and generation in ducts with flow, *J. Sound Vib.,* **14**(1), 37-55.

[2]. A. H. Nayfeh and M. Tsai, 1974. Nonlinear acoustic propagation in two-dimensional duct, *J. Acoust. Soc. Am.,* **55**(6), 1166-1172.

[3]. M. K. Myers, 1980. On the acoustic boundary condition in the presence of flow, *J. Sound Vib.,* **71**(3), 429-434.

[4]. L. Deike, M. Berhanu and E. Falcon, 2017. Experimental observation of hydroelastic three-wave interactions, *Phys. Rev. Fluids,* **2,** 064803.

[5]. S. Vijay Prakash and V. R. Sonti, 2016. Wave propagation in a 2D nonlinear structural acoustic waveguide using asymptotic expansion of wavenumbers, *J. Sound Vib.* **362,** 157-175.

[6]. B. Bharat and V. R. Sonti, 2020. Self and cross-mode interactions in a weakly nonlinear two-dimensional structural acoustic Waveguide, *J. Acoust. Soc. Am.* **147**(4), 2499-2510.

[7]. M. F. Hamilton and D. T. Blackstock, 1998. *Nonlinear Acoustics,* Academic Press. [8] M. L. Munjal, 2014. *Acoustics of Ducts and Mufflers*, Wiley.

[8]. K. S. Wang and P. G. Vaidya, 1975. Herrick Lab. Report No. HL - 75-35, Propagation of high amplitude higher order mode sounds in slightly soft rectangular ducts, carrying mean flow, Purdue University.

[9]. P. G. Vaidya, 1981. AIAA 7th Aeroacoustic Conference, Propagation of sound in flows containing mean flow gradient, Boeing Commercial Airplane Co.

[10]. T. W. Van Doren, 1993. PhD Thesis, Propagation of finite amplitude sound in multiple waveguide modes, The University of Texas and Austin, Texas.

INFORMATION FOR AUTHORS

ARTICLES

The Journal of Acoustical Society of India (JASI) is a refereed publication published quarterly by the Acoustical Society of India (ASI). JASI includes refereed articles, technical notes, letters-to-the-editor, book review and announcements of general interest to readers.

Articles may be theoretical or experimental in nature. But those which combine theoretical and experimental approaches to solve acoustics problems are particularly welcome. Technical notes, letters-to-the-editor and announcements may also be submitted. Articles must not have been published previously in other engineering or scientific journals. Articles in the following are particularly encouraged: applied acoustics, acoustical materials, active noise & vibration control, bioacoustics, communication acoustics including speech, computational acoustics, electro-acoustics and audio engineering, environmental acoustics, musical acoustics, non-linear acoustics, noise, physical acoustics, physiological and psychological acoustics, quieter technologies, room and building acoustics, structural acoustics and vibration, ultrasonics, underwater acoustics.

Authors whose articles are accepted for publication must transfer copyright of their articles to the ASI. This transfer involves publication only and does not in any way alter the author's traditional right regarding his/her articles.

PREPARATION OF MANUSCRIPTS

All manuscripts are refereed by at least two referees and are reviewed by the Publication Committee (all editors) before acceptance. Manuscripts of articles and technical notes should be submitted for review electronically to the Chief Editor by e-mail or by express mail on a disc. JASI maintains a high standard in the reviewing process and only accept papers of high quality. On acceptance, revised articles of all authors should be submitted to the Chief Editor by e-mail or by express mail.

Text of the manuscript should be double-spaced on A4 size paper, subdivided by main headings-typed in upper and lower case flush centre, with one line of space above and below and sub-headings within a section-typed in upper and lower case understood, flush left, followed by a period. Sub-sub headings should be italic. Articles should be written so that readers in different fields of acoustics can understand them easily. Manuscripts are only published if not normally exceeding twenty double-spaced text pages. If figures and illustrations are included then normally they should be restricted to no more than twelve-fifteen.

The first page of manuscripts should include on separate lines, the title of article, the names, of authors, affiliations and mailing addresses of authors in upper and lowers case. Do not include the author's title, position or degrees. Give an adequate post office address including pin or other postal code and the name of the city. An abstract of not more than 200 words should be included with each article. References should be numbered consecutively throughout the article with the number appearing as a superscript at the end of the sentence unless such placement causes ambiguity. The references should be grouped together, double spaced at the end of the article on a separate page. Footnotes are discouraged. Abbreviations and special terms must be defined if used.

EQUATIONS

Mathematical expressions should be typewritten as completely as possible. Equation should be numbered consecutively throughout the body of the article at the right hand margin in parentheses. Use letters and numbers for any equations in an appendix: Appendix A: (A1, (A2), etc. Equation numbers in the running text should be enclosed in parentheses, i.e., Eq. (1), Eqs. (1a) and (2a). Figures should be referred to as Fig. 1, Fig. 2, etc. Reference to table is in full: Table 1, Table 2, etc. Metric units should be used: the preferred from of metric unit is the System International (SI).

REFERENCES

The order and style of information differs slightly between periodical and book references and between published and unpublished references, depending on the available publication entries. A few examples are shown below.

Periodicals:

[1] S.R. Pride and M.W. Haartsen, 1996. Electroseismic wave properties, *J. Acoust. Soc. Am.*, **100** (3), 1301-1315.

[2] S.-H. Kim and I. Lee, 1996. Aeroelastic analysis of a flexible airfoil with free play non-linearity, *J. Sound Vib.*, **193** (4), 823-846.

Books:

[1] E.S. Skudzryk, 1968. *Simple and Comlex Vibratory Systems*, the Pennsylvania State University Press, London.

[2] E.H. Dowell, 1975. *Aeroelasticity of plates and shells*, Nordhoff, Leyden.

Others:

[1] J.N. Yang and A. Akbarpour, 1987. Technical Report NCEER-87-0007, Instantaneous Optimal Control Law For Tall Buildings Under Seismic Excitations.

SUMISSIONS

All materials from authors should be submitted in electronic form to the JASI Chief Editor: B. Chakraborty, CSIR - National Institute of Oceanography, Dona Paula, Goa-403 004, Tel: +91.832.2450.318, Fax: +91.832.2450.602,(e-mail: bishwajit@nio.org) For the item to be published in a given issue of a journal, the manuscript must reach the Chief Editor at least twelve week before the publication date.

SUMISSION OF ACCEPTED MANUSCRIPT

On acceptance, revised articles should be submitted in electronic form to the JASI Chief Editor (bishwajit@nio.org)